The Resolution Dependence of Explicitly Modeled Convective Systems

MORRIS L. WEISMAN, WILLIAM C. SKAMAROCK, AND JOSEPH B. KLEMP

National Center for Atmospheric Research, Boulder, Colorado*

(Manuscript received 7 December 1995, in final form 22 July 1996)

ABSTRACT

The representation of convective processes within mesoscale models with horizontal grid sizes smaller than 20 km has become a major concern for the simulation of mesoscale weather systems. In this paper, the authors investigate the effects of grid resolution on convective processes using a nonhydrostatic cloud model to help clarify the capabilities and limitations of using explicit physics to resolve convection in mesoscale models. By varying the horizontal grid interval between 1 and 12 km, the degradation in model response as the resolution is decreased is documented and the processes that are not properly represented with the coarser resolutions are identified.

Results from quasi-three-dimensional squall-line simulations for midlatitude-type environments suggest that resolutions of 4 km are sufficient to reproduce much of the mesoscale structure and evolution of the squall-line-type convective systems produced in 1-km simulations. The evolution at coarser resolutions is characteristically slower, with the resultant mature mesoscale circulation becoming stronger than those produced in the 1-km case. It is found that the slower evolution in the coarse-resolution simulations is largely a result of the delayed strengthening of the convective cold pool, which is crucial to the evolution of a mature, upshear-tilted convective system. The relative success in producing realistic circulation patterns at later times for these cases occurs because the cold pool does eventually force the system to grow upscale, allowing it to be better resolved. The stronger circulation results from an overprediction of the vertical mass transport produced by the convection at the leading edge of the system, due to the inability of the coarse-resolution simulations to properly represent nonhydrostatic effects.

1. Introduction

One of the ongoing concerns in the simulation of weather systems with mesoscale models is how to represent subgrid-scale convective processes as horizontal grid intervals continue to decrease. Convective parameterizations are clearly necessary for resolutions between 20 and 50 km (e.g., Frank 1983; Molinari and Dudek 1992), but traditional approaches based on scale separation (e.g., Ooyama 1971; Anthes 1977), which form the basis for most currently used parameterization schemes, are not well posed theoretically for such applications, and have, not surprisingly, met with only limited success. For such resolutions, individual convective elements may be comparable in size to the mesoscale grid volume and can have life cycles that are of the same order as the timescales of other resolved features. Furthermore, these individual convective elements often build upscale to produce organized mesoscale convective systems of 100 km size or greater. Although mesoscale models can, in principal, partially resolve these systems explicitly, the convective processes that drive the circulations are still unresolved and must be parameterized in some way. As grid intervals decrease below 20 km, the problems become even more complex as the convective elements themselves may become partially resolved. However, it is still unclear what resolution is necessary to represent the convective processes sufficiently to avoid parameterization altogether.

Over the past decade, nonhydrostatic cloud model simulations employing grid resolutions of 2 km or less have shown much success in replicating the observed structure and evolution of convection, including the upscale growth from individual convective cells to full mesoscale convective systems (e.g., Rotunno et al. 1988; Weisman et al. 1988; Lafore and Moncrieff 1989; Weisman 1992, 1993; Skamarock et al. 1994). These studies have established a strong basis of understanding of the physical processes important to the evolution of convective systems that can be used to help determine how convection should be represented in coarser-grid mesoscale models.

In this paper, we begin a study of the representation of convection within mesoscale models by investigating the effects of horizontal grid size on explicitly resolved

*The National Center for Atmospheric Research is sponsored by the National Science Foundation.

Corresponding author address: Dr. Morris L. Weisman, NCAR, P.O. Box 3000, Boulder, CO 80307-3000.
E-mail: weisman@ncar.ucar.edu

convective processes using a nonhydrostatic cloud model. Specifically, we consider resolutions between 1 and 12 km in light of the increasing trend for mesoscale models to be applied at these finer scales. We also limit our discussions to timescales of 6 h or less to emphasize issues related to the short-term forecasting of convection and convective systems. This further allows us to avoid issues related to Coriolis effects, which play a role in the evolution of longer-lived convective systems. In all cases, the 1-km resolution simulation is used to represent the ''ground truth'' from which to judge the coarser resolution results.

In this study, we attempt to document the dependence of the model response on the resolution given that convection is triggered, and identify the processes that are not properly represented at the coarser resolutions. We believe that the knowledge gained from this study will be helpful in identifying new approaches to convective parameterization over this range of grid scales. This approach also allows us to more clearly determine the minimum resolution necessary to accurately represent the convective processes explicitly. We do not attempt to evaluate the various existing convective parameterization schemes, nor do we attempt to address the issues related to convective initiation or the interaction between the convection and larger-scale features, all of which are important concerns.

For this initial study, we investigate the effects of resolution on the evolution of quasi-two-dimensional squall lines, as described by Weisman et al. (1988, hereafter WKR) and Rotunno et al. (1988, hereafter RKW). These systems have been chosen since much is known observationally about their structure and evolution, and since they have been investigated extensively using both fine-grid nonhydrostatic and coarse-grid hydrostatic models. Also, squall lines represent one of the most commonly observed forms of mesoscale organization for convective systems, thus providing a good test of the ability of a model to represent the upscale growth from convective to mesoscale processes. We specifically use thermodynamic conditions associated with strong, midlatitude systems that, together with three different representative ambient shear profiles, reproduce much of the range of observed squall-line behavior.

Our goals are to first determine the minimum grid resolution necessary to explicitly simulate squall-line-type systems. This is accomplished by comparing the system-scale structure (section 3) and key system-averaged statistics (section 4) among the various simulations with differing resolutions. These results suggest that 4-km resolution is sufficient to reproduce most system-scale aspects of squall-line behavior over a 6-h period, with resolutions of 8 km or larger resulting in significantly slower system evolution and stronger system-scale circulation. We then analyze these results in terms of hydrostatic scaling arguments (section 5), which help demonstrate why the slower evolution and stronger circulation occur for the coarser resolutions. Finally, in section 6, we discuss the implications and limitations in applying these results to improve the representation of convective processes over this range of resolution.

2. Model formulation and experimental design

The simulations described in this study were conducted using the three-dimensional nonhydrostatic numerical cloud model described by Klemp and Wilhelmson (1978), as also used by Weisman et al. (1988). The model does not include ice processes or radiative heating. Open boundary conditions are employed on the lateral boundaries in the cross-line (east–west) direction, with periodic conditions specified in the along-line (north–south) direction. A gravity wave radiation condition is employed at the upper boundary (Klemp and Durran 1983), with a free-slip condition specified at the surface. The Coriolis force is set to zero to simplify the interpretation of the results. This simplification will have minimal effects on the simulations over the first 3–4 h, but may have some impact on the interpretation of the results at 6 h and beyond, by which point the Coriolis forcing may generate significant across-line shear for quasi-two-dimensional lines (e.g., Fovell 1991) or mesoscale convective vortices for finite-length squall lines (e.g., Skamarock et al. 1994). In light of this, we have run additional simulations that confirm that the inclusion of Coriolis effects does not significantly alter the results reported herein.

Convective initiation is an integral part of both convective resolving simulations as well as convective parameterizations. We do not address the convective initiation problem specifically here, but rather seek to determine how the convection evolves as a function of resolution once it is initiated. Therefore, we have sought an initiation procedure that provides similar convective forcing across the range of resolutions considered. Although this is not entirely possible, Klemp et al. (1994), among others, have shown that the properties of gravity currents are well described by the hydrostatic equations. One of the implications of such hydrostatic behavior is that a spreading cold pool will produce a vertical mass flux at its leading edge that is nearly independent of grid resolution, thus providing similar convective triggering for all of the simulations.

Based on this, we have chosen to initiate the quasi-three-dimensional squall lines using a 2-km-deep semi-infinite cold pool, with the maximum potential temperature deficit at the surface set at -8 K, decreasing linearly to zero at 2 km AGL (Fig. 1). As integrations proceed, strong potential temperature gradients at the leading edge of the cold pool collapse to the grid scale for all horizontal resolutions under consideration. Convection is triggered as the cold pool begins to spread against the ambient flow, inducing surface convergence and upward motion along the leading edge of the cold air. The addition of small random temperature pertur-

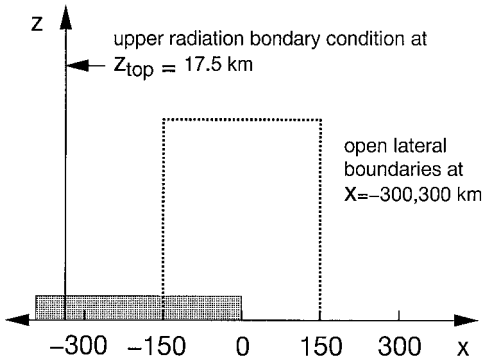

FIG. 1. Domain layout for squall-line simulations. Shading depicts the initial location of the surface cold pool, which is prescribed to be 2.5 km deep with a maximum potential temperature deficit of 8°C at the surface, decreasing linearly to zero at 2.5 km.

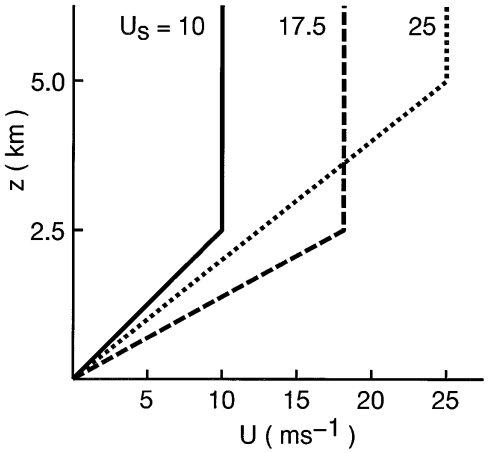

FIG. 2. Vertical wind shear profiles used in model simulations, depicting (a) $U_s = 10$ m s^{-1} over 2.5 km, (b) $U_s = 17.5$ m s^{-1} over 2.5 km, and (c) $U_s = 25$ m s^{-1} over 5 km AGL.

bations along the leading edge of the cold air allows for the development of three-dimensional cellular structures along the line. This initialization procedure is consistent with the observed scenario of a squall line being triggered by a preexisting mesoscale temperature boundary, such as a cold front or cold outflow produced by prior convection. However, in this initial study, we do not consider any further interactions between the new convection and such larger-scale features.

Each simulation is run within a physical domain that is 600 km in the cross-line (x) direction, 160 km in the along-line (y) periodic direction, and 17.5 km in the vertical. The only exceptions are the 1-km resolution simulations, for which the along-line dimension is limited to 120 km due to computer memory constraints. Based on our past experiences, a 600-km domain in the cross-line direction is large enough to assure an essentially domain-independent solution over the time frame being considered. The vertical resolution is set at 700 m, with the horizontal resolution ranging between 1, 2, 4, 8, and 12 km. Tests were also run using a stretched grid in the vertical, with vertical resolutions varying from 350 m at the surface to over 1 km at the top of the domain, but the use of vertical stretching did not significantly affect the presented results. All simulations are run for 6 h, with the exception of the 12-km resolution experiments, which are run an additional 3 h.

One of the more problematic issues faced in designing the present set of experiments was how to specify the physical and computational mixing coefficients so that mixing-dependent sensitivities do not strongly influence the results across the range of resolutions being considered. In the model formulation being used, the ''physical mixing,'' which is specified via the mixing coefficient K_m, is determined prognostically through the use of a turbulence energy equation, and scales with the horizontal resolution. However, the ''computational mixing,'' which is represented primarily by a fourth-order smoother and which is necessary to maintain numerical stability of the solutions, maintains the same rate of smoothing for $2\Delta x$ (and $4\Delta x$, etc.) waves over the full range of resolutions, and, thus, does not produce the same net magnitude of smoothing over the range of resolutions. One could argue that the same amount of smoothing should be maintained over the range of resolutions for a fair comparison among the cases. This makes sense for the physical mixing, but the primary goal of the computational smoothing is to maintain numerical stability of the solution, which is accomplished by reducing the amplitude of the $2\Delta x$ features that are not properly represented for the given grid size. The consequence of not smoothing $2\Delta x$ features sufficiently is the production of gridpoint scale numerical noise, which does not represent the true physical solution, and which can lead to numerical instability. From this perspective, maintaining the same rate of smoothing for the $2\Delta x$ waves seems to be the appropriate approach to take. These mixing formulations are discussed further in the appendix, where we demonstrate that the presented resolution dependencies are not affected significantly by the mixing formulations chosen for our experiments.

Three different environmental vertical wind shear profiles are considered (see Fig. 2) that reproduce a large range of observed squall-line behavior. For two of the cases, a linear shear profile is prescribed between the surface and 2.5 km AGL, with constant winds aloft. The maximum magnitude of the wind in the profile is set at either $U_s = 10$ m s^{-1} or $U_s = 17.5$ m s^{-1}. For the weaker-shear case, an initial line of strong convective cells quickly gives way to a shallower upshear-tilted mesoscale circulation associated with the storm-induced cold pool. For the stronger-shear case, however, strong leading-line convection is maintained for several hours before giving way to the upshear-tilted mesoscale circulation. An additional case considers a deeper shear profile, with the wind shear extending up to 5 km AGL and the maximum magnitude of the wind set at U_s =

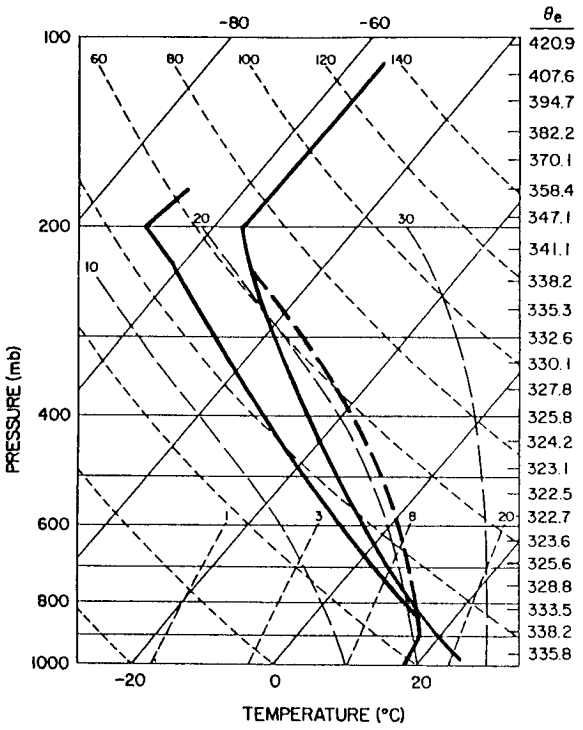

FIG. 3. Initial temperature and moisture sounding used in model simulations.

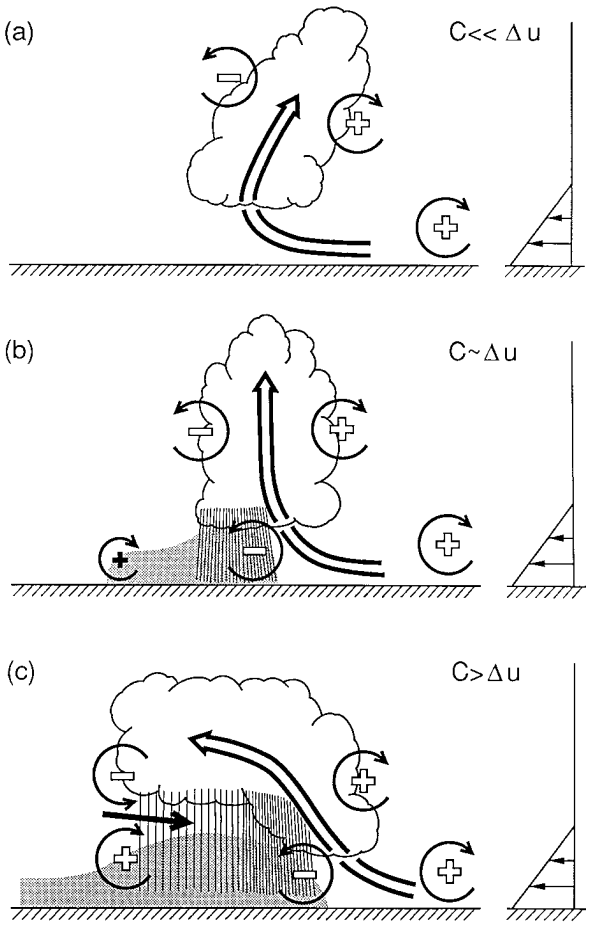

FIG. 4. Three stages in the evolution of a convective system. The system tilt evolves through a (a) downshear, (b) vertical, and (c) upshear orientation over time. From Weisman (1992).

25 m s^{-1}. This case maintains strong leading-line convective cells throughout the simulation and does not develop the upshear-tilted mesoscale circulation evident in the shallower shear cases. The thermodynamic sounding for each case is the same as used in WKR (Fig. 3), and contains a moderate amount of convective available potential energy (CAPE = 2400 m^2 s^{-2}) and generally moist conditions throughout the troposphere. These thermodynamic conditions are most closely associated with severe, midlatitude squall lines (e.g., Bluestein and Jain 1985).

3. Overall system evolution

We shall illustrate the dependence of the basic evolution of the convective systems on resolution by comparing the overall system structure for the 1- and 12-km resolution simulations for the various shear cases. Since we are most interested in comparing the resultant mesoscale structures rather than cellular-scale structures, we present vertical cross sections of key along-line averaged quantities at 3 and 6 h. We also present cross sections at 9 h for the 12-km resolution simulations to emphasize differences in the timing of the evolution for the coarser resolution cases. In all cases, only the central 312 km of the full 600-km domain dimensions in x is displayed.

For all simulations, the initial cold pool spreads along the surface and weakens during the first hour as it mixes with the ambient air, with the maximum temperature deficits decreasing to less than 4 K near the leading edge of the outflow. However, the convergence and lifting produced by this spreading cold pool triggers convective cells that subsequently enhance the cold pool through both the evaporation of rainfall and through the transport of potentially colder and drier midlevel air to the surface via the rain-induced downdrafts. As described by RKW and WKR, the initial convective cells develop an upright-to-downshear tilted circulation in response to the ambient vertical wind shear. However, as the cold pool strengthens, the cold-pool circulation eventually overwhelms the ambient shear, forcing the convective circulation to be tilted predominantly upshear, as depicted in Fig. 4.

The development of the upshear-tilted circulation represents the critical step in the development of the mature mesoscale squall-line structure, composed of a warm, ascending front-to-rear updraft current and a cold, descending rear-inflow current and associated surface cold pool (e.g., Houze et al. 1989). The temperature perturbations associated with this flow configuration are es-

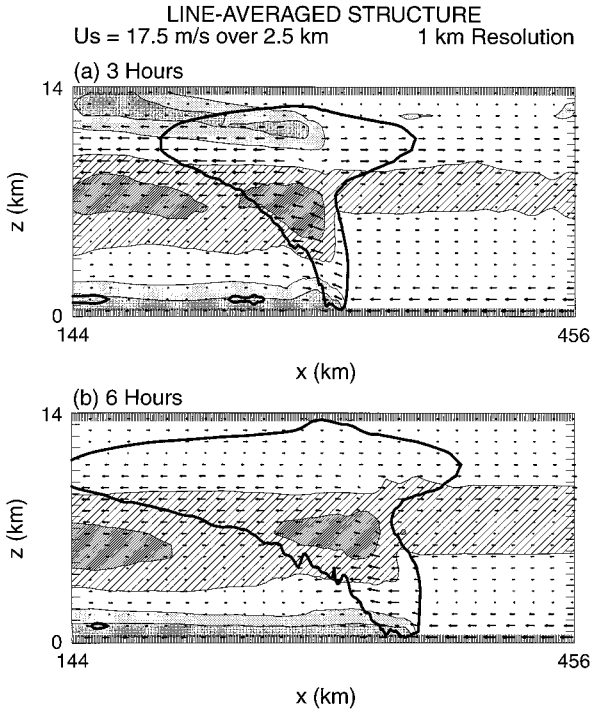

FIG. 5. Vertical cross sections for the 1-km resolution, $U_s = 17.5$ m s^{-1} simulation at (a) 3 and (b) 6 h. The perturbation potential temperature field is contoured every 2 K (zero contour omitted), with perturbations greater than 2 and 4 K shaded with light and dark diagonal lines and perturbations greater than -2 and -4 K shaded with light and dark stippling, respectively. Vectors are presented every 12 km, with a distance of 12 km equal to a vector magnitude of 22.5 m s^{-1}. A domain speed of $u = 17.5$ m s^{-1} has been subtracted from the vector field (i.e., approximately storm relative). The thick solid line represents the outline of the cloud water field.

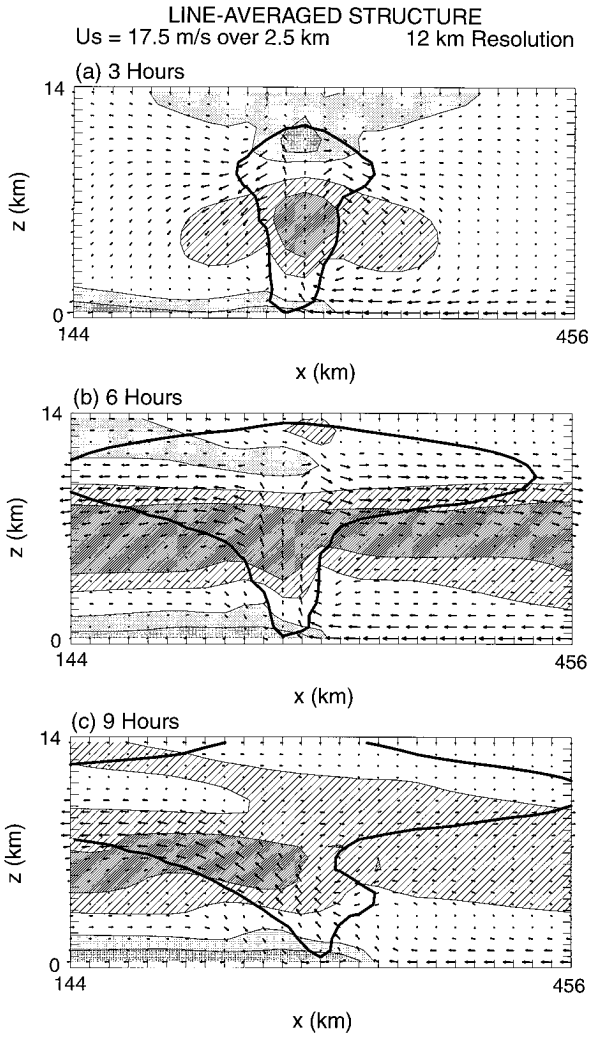

FIG. 6. Same as in Fig. 5 except for the 12-km resolution, $U_s = 17.5$ m s^{-1} simulation at (a) 3, (b) 6, and (c) 9 h.

sentially in hydrostatic balance, and, as such, are also associated with the mesoscale pressure perturbations that produce and maintain much of the system-scale circulation (e.g., Lafore and Moncrieff 1988; Weisman 1992). As described by WKR and Weisman (1992), the strength and timing of the evolution of these features depends on both the magnitude of the environmental instability, which controls the potential magnitude of the temperature perturbations in the updraft and downdraft, and the strength of the ambient vertical wind shear, which controls the ability of the system to develop the upshear-tilted structure. This description of system evolution, along with its dependencies on environmental conditions, serves as the basic physical model that we use to interpret the resolution-dependencies depicted in the various simulations.

a. Moderate, shallow shear

We will first consider the $U_s = 17.5$ m s^{-1} shallow shear case, which replicates many features of observed long-lived squall lines, and which clearly demonstrates the resolution dependencies evident in the various simulations. By 3 h (Fig. 5a), the 1-km resolution convective system has reached a quasi-steady mature state (e.g., Fig. 4c) consisting of a strong, deep cold pool and outflow at the surface, with a narrow zone of intense updraft at the leading edge of the system with more gradual ascent as air spreads and accelerates rearward above the cold air. A rear-inflow jet has developed at midlevels (e.g., Weisman 1992) that helps supply the potentially cold and dry air necessary for the maintenance of the downdraft circulation. The main updraft current at midlevels is as much as 5 K warmer than the ambient environment, with a zone of greater than 2 K of warming also extending ahead of the system beneath the anvil aloft. Warming near the center and to the rear of the system is associated primarily with the upward transport of potentially warm air from near the surface by the updraft current, while ahead of the system, warming is due primarily to the compensating subsidence produced in response to the divergence at the top of the storm.

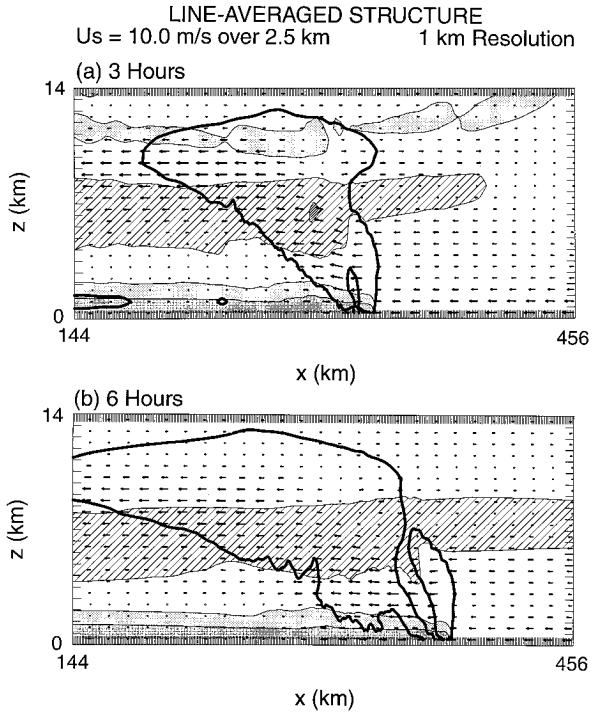

FIG. 7. Same as in Fig. 5 except for the 1-km resolution, U_s = 10.0 m s^{-1} simulation at (a) 3 and (b) 6 h. A domain speed of u = 12.5 m s^{-1} has been subtracted from the vector field.

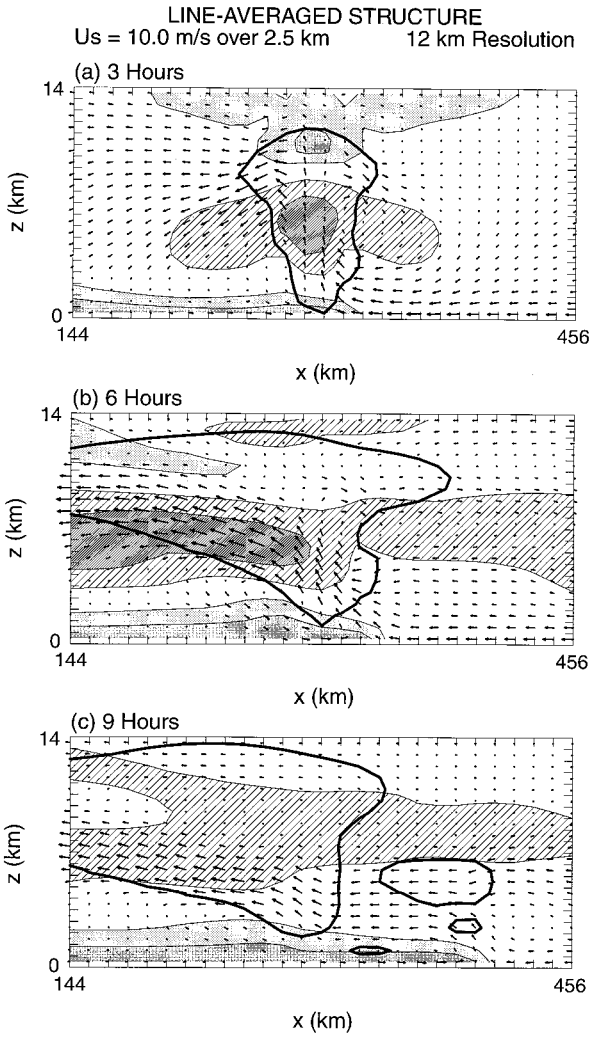

FIG. 8. Same as in Fig. 5 except for the 12-km resolution, U_s = 10.0 m s^{-1} simulation at (a) 3, (b) 6, and (c) 9 h. A domain speed of u = 12.5 m s^{-1} has been subtracted from the vector field.

This basic structure is maintained through 6 h (Fig. 5b) and beyond.

The evolution of the 12-km resolution simulation (Fig. 6) is similar, but much slower than that depicted for the 1-km case. At 3 h (Fig. 6a), the system is composed of a broad zone of weak updraft that produces a nearly symmetric outflow aloft (as in Fig. 4b). The cold pool at the surface is also much weaker and shallower than the above case, but a zone of greater than 2 K of subsidence warming is evident at midlevels extending to both sides of the system. Between 3 and 6 h, the cold pool strengthens and deepens somewhat, with the updraft becoming much broader and deeper while still producing a symmetric outflow aloft (Fig. 6b). The zone of midlevel warming both ahead and behind the system is also much greater than at 3 h. In addition, a rear-inflow jet as well as enhanced inflow from the front of the system has developed at midlevels.

The cold pool continues to strengthen and deepen after 6 h, and by 9 h the convective system has developed an upshear-tilted structure with a broad front-to-rear ascending current located above a descending rear-inflow jet (Fig. 6c; as in Fig. 4c). In addition, the midlevel warming ahead of the system has decreased significantly, although a large zone of greater than 4 K of warming is still evident spreading rearward at midlevels within the front-to-rear ascending current. The overall structure of the 12-km resolution simulation by 9 h (Fig. 6c) resembles the structure produced in the 1-km resolution simulation at both 3 and 6 h (Figs. 5a,b).

b. Weak, shallow shear

For this set of simulations, the vertical wind shear is again confined to the lowest 2.5 km AGL, but the magnitude of the change in wind speed is weakened to U_s = 10 m s^{-1}. With the weaker shear, the cold pool generates an upshear-tilted circulation earlier in the 1-km resolution simulation, producing a shallower and weaker front-to-rear ascending current over the cold pool by 3 h, with almost no midlevel rear inflow at the back edge of the system (Fig. 7a). The temperature perturbations aloft are also weaker, with generally less than 4-K warming in the front-to-rear flow, and only a small area of 2-K warming ahead of the system. The front-to-rear circulation becomes even shallower by 6 h (Fig. 7b),

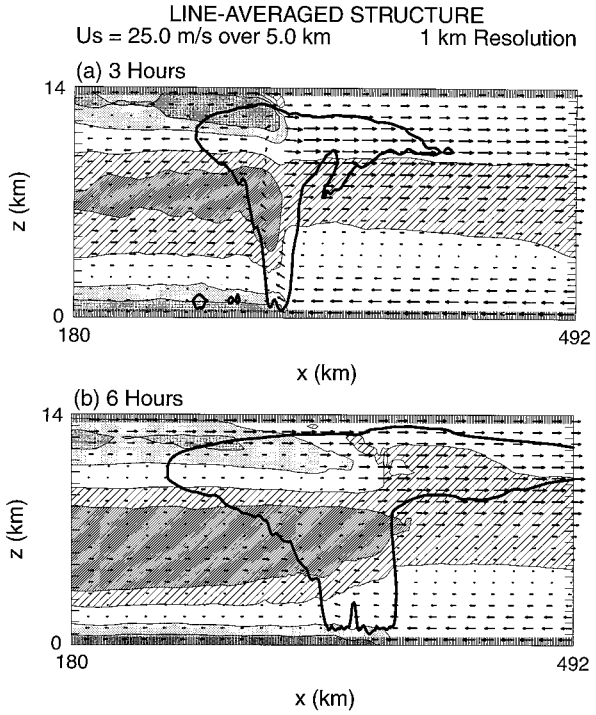

FIG. 9. Same as in Fig. 5 except for the 1-km resolution, U_s = 25.0 m s^{-1} simulation at (a) 3 and (b) 6 h. A domain speed of u = 18 m s^{-1} has been subtracted from the vector field.

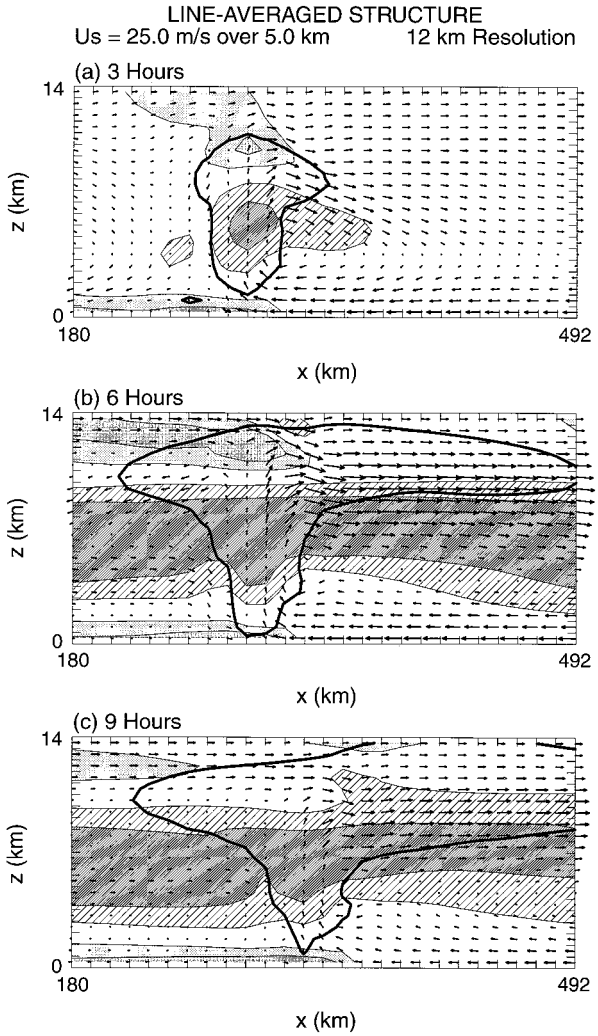

FIG. 10. Same as in Fig. 5 except for the 12-km resolution, U_s = 25.0 m s^{-1} simulation at (a) 3, (b) 6, and (c) 9 h. A domain speed of u = 18 m s^{-1} has been subtracted from the vector field.

with about the same amount of warming aloft, except that the warming extends further ahead of the system. The weaker circulation and associated temperature perturbations aloft for weaker ambient shears are consistent with the previous results of WKR and Weisman (1992).

As with the stronger shear case, the 12-km resolution simulation is again much slower to evolve to the mature state than the 1-km case. At 3 h (Fig. 8a), the system is still composed of a broad, upright, and symmetric updraft current, with a core of greater than 4-K temperature perturbations centered on the updraft and greater than 2-K perturbations extending to both sides of the updraft, associated with the compensating subsidence. By 6 h (Fig. 8b), the system has developed a prominent upshear tilt, with a broad, warm ascending front-to-rear flow and descending rear-inflow beneath. As in the stronger shear case, the front-to-rear flow is much stronger and warmer than in the 1-km simulation. By 9 h (Fig. 8c), the overall structure and magnitude of the wind and temperature perturbations are again similar to those in the 1-km case at 6 h (Fig. 7b).

c. Deeper shear

For this set of simulations, the depth of the ambient shear layer is increased to 5 km AGL, with the magnitude of the wind at the top of the shear layer increased to U_s = 25 m s^{-1}. With this magnitude and depth of shear, the initial and subsequent convectively produced cold pool is too weak to overcome the effects of the shear, and the 1-km resolution convective system remains upright-to-downshear tilted throughout the 6 h simulation (Fig. 9; as in Fig. 4a). Although the outflow in the anvil aloft spreads predominantly downshear, a broad zone of greater than 4 K of subsidence warming still extends upshear of the main updraft region.

The 12-km simulation is again slower to evolve, and although the basic structure by 6 h (Fig. 10b) looks similar to the 1-km simulation at 6 h, the downshear outflow within the anvil is much stronger than in the 1-km simulation and produces substantially more subsidence warming. Extending the 12-km simulation to 9 h (Fig. 10c) improves the comparison with the anvil-wind magnitudes somewhat, but the midlevel warming downshear of the system remains substantially greater than in the 1-km resolution simulation (Fig. 9b).

4. System-average statistics

To quantify these results for the entire range of resolutions used, we present system-averaged vertical profiles of several significant quantities at 3 and 6 h. A 200-km averaging region has been chosen for this analysis, centered on the leading edge of the gust front. This includes the primary leading-edge convective zone, a substantial portion of the stratiform circulation to the rear, as well as the most significant region of downshear influence.

a. Heat and momentum fluxes

We begin by presenting profiles of $w'\theta'$ and $w'u'$, which represent some of the typical terms from the Reynolds-averaged equations that must be represented in standard convective parameterization schemes (e.g., Anthes 1977). In the present context, however, these terms should not be interpreted as heat or momentum transports that would be used for such schemes in mesoscale models. Such schemes operate on single grid volumes with grid lengths generally of 20–50 km, while the current averaging extends over a number of these grid volumes. The purpose here is to characterize the system-scale structure and evolution in a meaningful, quantitative fashion. Recent numerical studies by Schlesinger (1990, 1994) do address such parameterization issues more directly for isolated convective cells for both midlatitude and tropical environments.

The averaged vertical profiles of $w'\theta'$ and $w'u'$ at 3 and 6 h for the three different shear profiles are presented in Figs. 11 and 12, respectively. At 3 h, the vertical profiles for the 1-km resolution base simulations depict a maximum in the vertical heat flux and minimum in the vertical momentum flux at about 7 km AGL, which is generally consistent with the development of a mature, upshear-tilted circulation. In addition, the magnitudes of these flux profiles increase with increasing strength and/or depth of the vertical wind shear, reflecting the positive influence of stronger vertical wind shear on overall squall-line strength (e.g., RKW, WKR).

Both the shape and magnitude of the vertical heat flux and vertical momentum flux profiles for the shallow-shear experiments are reproduced quite well in the 2-km and 4-km resolution simulations at 3 h, but the results deteriorate somewhat in the 4-km resolution deeper-shear simulation, and even more significantly for all of the shear experiments as the resolution is decreased further. The coarser resolutions overpredict the averaged vertical heat flux while significantly underpredicting the vertical momentum flux. This is consistent with the coarser-resolution simulations developing the mature, upshear-tilted circulations more slowly than in the finer-resolution simulations. The slower evolution for the coarse-resolution simulations is especially evident for the deeper-shear case, where even the vertical heat flux is lagging the finer-resolution results at 3 h.

By 6 h, the 1-km resolution vertical-flux magnitudes have all weakened (Figs. 11d–f and 12d–f). This evolution is consistent with the slow weakening of the convective systems as the circulations become shallower and more strongly tilted upshear. At this time, the 2- and 4-km results are comparable to the 1-km results for all three shear cases, while the coarser resolutions generally overpredict the vertical heat fluxes. However, the vertical momentum fluxes are now similar for most of the resolutions presented, which is consistent with all the simulations depicting a more mature, upshear-tilted circulation. The exception, again, is the deeper-shear case, which still exhibits weaker vertical momentum fluxes for the coarser resolutions. As at earlier times, the magnitudes of the flux profiles increase for increasing magnitude and/or depth of the vertical wind shear.

b. Moisture statistics

The average perturbation water vapor mixing ratio $\overline{q_v'}$ is also useful in characterizing the overall structure of the convective system (Fig. 13). At 3 h, the profiles of $\overline{q_v'}$ for the 1-km simulations all show significant drying in the lower 3 km associated with the descending rear-inflow jet, and moistening above associated with the ascending front-to-rear flow in the anvil region. The 2- and 4-km resolution profiles are almost identical to the 1-km case for the shallow shear cases, while the coarser resolutions depict generally less drying below and less moistening above. For the deeper shear case, the 4- and 8-km resolution simulations produce less drying at low levels, with the 12-km case actually moistening through most of the depth of the profile.

By 6 h, the 1-km simulations all show more moistening aloft relative to earlier, due to the development of a more mature upshear-tilted circulation. All of the resolutions now produce similar results for the $U_s = 10$ m s^{-1} shallow shear case, and all but the 12-km resolution case produce similar results for the $U_s = 17.5$ m s^{-1} environment, which still displays less drying at low levels. However, all of the coarser resolutions display less drying at low levels for the $U_s = 25$ m s^{-1} deeper shear case.

Rainfall represents one of the more critical parameters that must be forecast by a mesoscale model. Averaged profiles of rainfall mixing ratios, $\overline{q_r}$, are presented for the three shear experiments and for all the resolutions in Fig. 14. For this discussion, $\overline{q_r}$ is averaged only over the 100-km region upshear of the gust front, since very little rain falls downshear of this location. At 3 h, the rainfall mixing ratios for the 1-km resolution simulations exhibit a maximum aloft, with the overall magnitude and height of maximum $\overline{q_r}$ increasing with increasing magnitude of the vertical wind shear. The 1-, 2-, and 4-km resolution results are quite similar for all the shears, but $\overline{q_r}$ for the coarser resolutions increase significantly in both of the shallower shear simulations. This result is consistent with the generally larger vertical

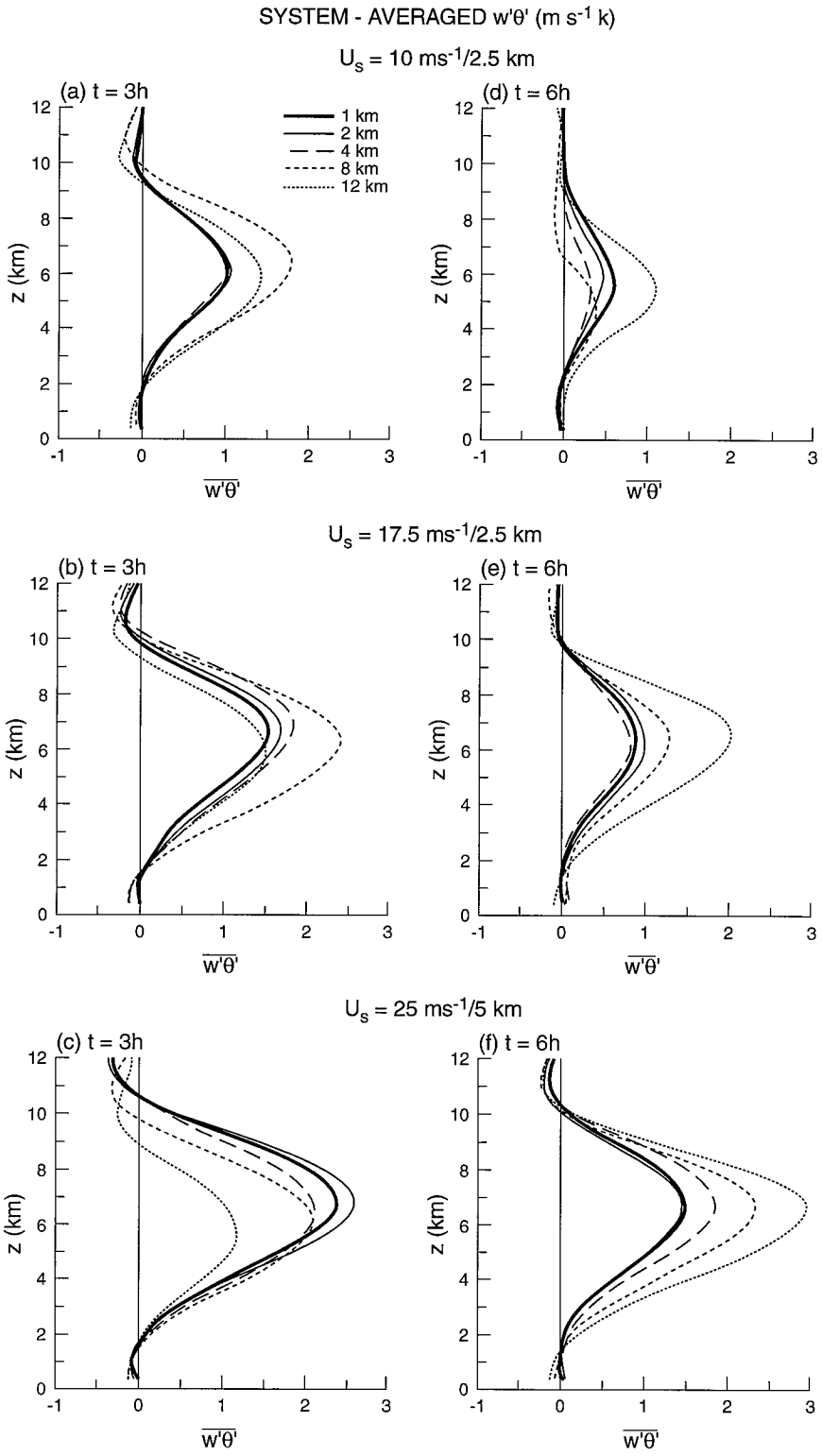

FIG. 11. Line-averaged vertical profiles of $w'\theta'$ for resolutions of 1, 2, 4, 8, and 12 km for the (a, d) U_s = 10 m s^{-1} (2.5 km)$^{-1}$, (b, e) U_s = 17.5 m s^{-1} (2.5 km)$^{-1}$, and (c, f) U_s = 25 m s^{-1} (5 km)$^{-1}$ simulations at 3 and 6 h, respectively. The 1-km resolution simulation is depicted by a thick solid line, 2 km by a thin solid line, 4 km by a large-dashed line, 8 km by a small-dashed line, and 12 km by a dotted line. All averages are calculated over a 200-km area centered on the surface cold-pool boundary.

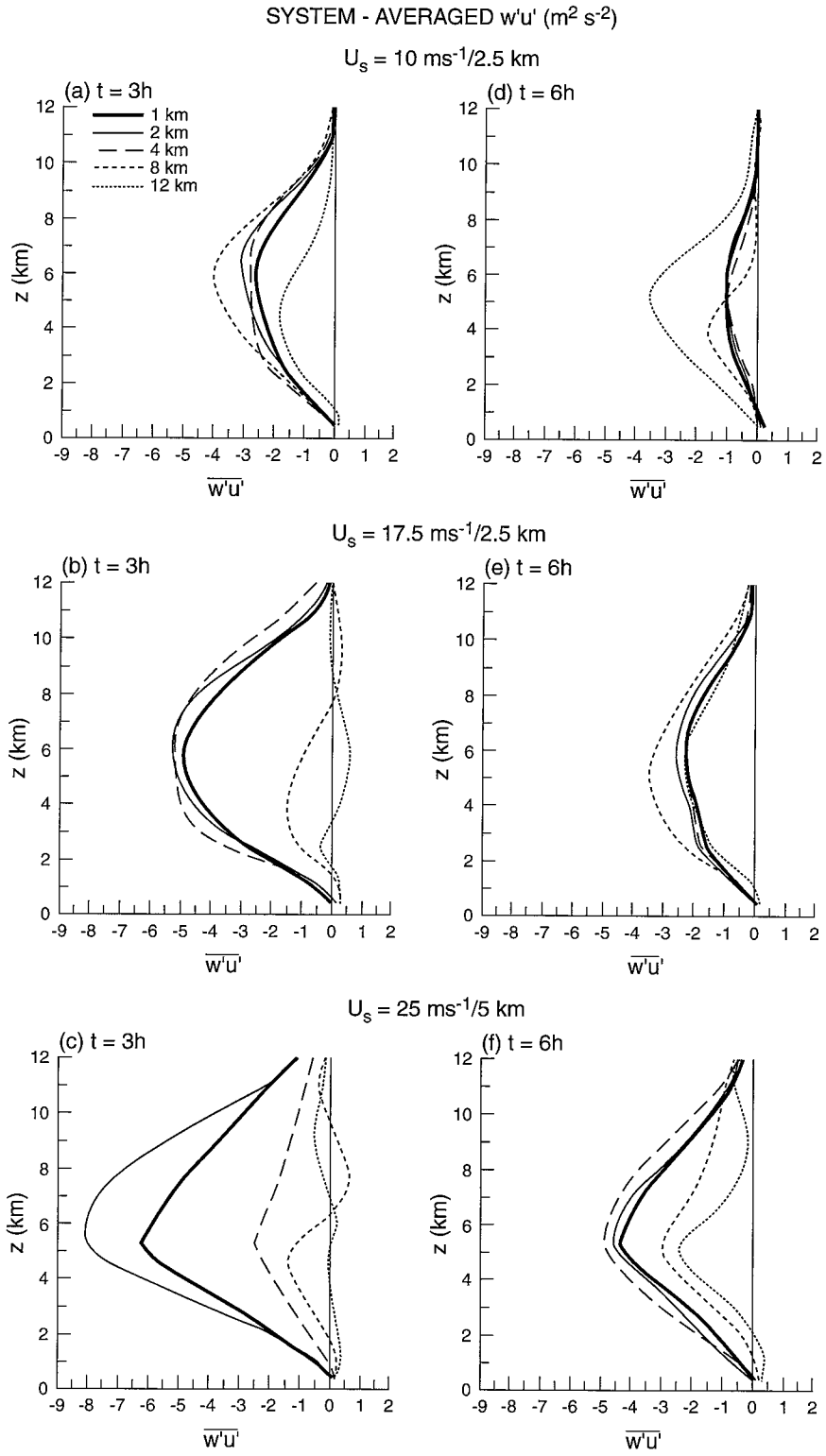

FIG. 12. Line-averaged vertical profiles of $w'u'$ for resolutions of 1, 2, 4, 8, and 12 km for the (a, d) U_s = 10 m s^{-1} (2.5 km)$^{-1}$, (b, e) U_s = 17.5 m s^{-1} (2.5 km)$^{-1}$, and (c, f) U_s = 25 m s^{-1} (5 km)$^{-1}$ simulations at 3 and 6 h, respectively. The 1-km resolution simulation is depicted by a thick solid line, 2 km by a thin solid line, 4 km by a large-dashed line, 8 km by a small-dashed line, and 12 km by a dotted line. All averages are calculated over a 200-km area centered on the surface cold-pool boundary.

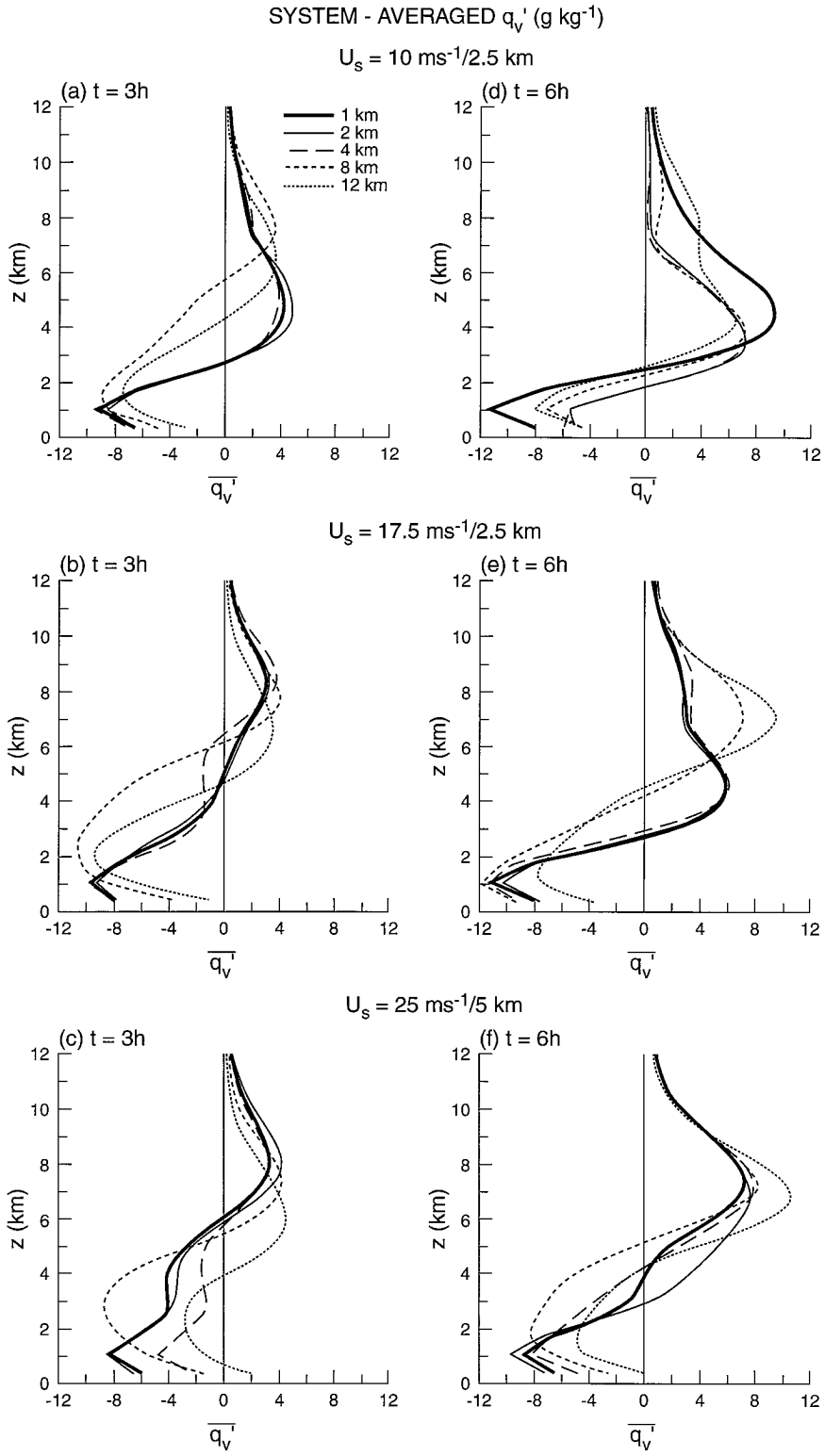

FIG. 13. Line-averaged vertical profiles of q_v' for resolutions of 1, 2, 4, 8, and 12 km for the (a, d) U_s = 10 m s^{-1} (2.5 km)$^{-1}$, (b, e) U_s = 17.5 m s^{-1} (2.5 km)$^{-1}$, and (c, f) U_s = 25 m s^{-1} (5 km)$^{-1}$ simulations at 3 and 6 h, respectively. The 1-km resolution simulation is depicted by a thick solid line, 2 km by a thin solid line, 4 km by a large-dashed line, 8 km by a small-dashed line, and 12 km by a dotted line. All averages are calculated over a 200-km area centered on the surface cold-pool boundary.

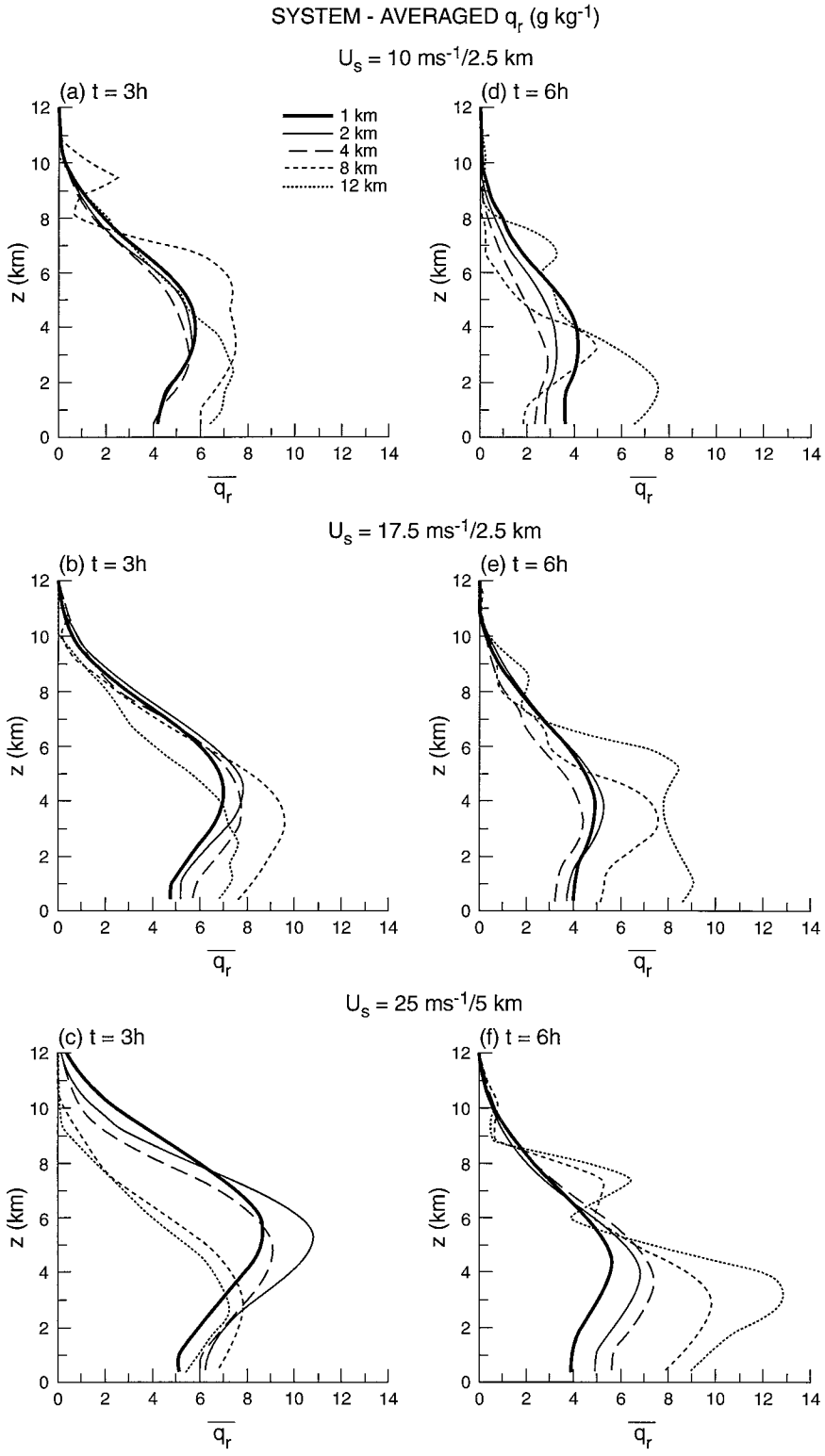

FIG. 14. Line-averaged vertical profiles of q_r for resolutions of 1, 2, 4, 8, and 12 km for the (a, d) U_s = 10 m s^{-1} (2.5 km)$^{-1}$, (b, e) U_s = 17.5 m s^{-1} (2.5 km)$^{-1}$, and (c, f) U_s = 25 m s^{-1} (5 km)$^{-1}$ simulations at 3 and 6 h, respectively. The 1-km resolution simulation is depicted by a thick solid line, 2 km by a thin solid line, 4 km by a large-dashed line, 8 km by a small-dashed line, and 12 km by a dotted line. All averages are calculated over a 100-km area extending rearward from the surface cold-pool boundary.

TABLE 1a. Moisture statistic: $T = 3$ h.

Resolution (km)	Total condensation ($\times 10^{12}$ kg)	Cloud water evaporation ($\times 10^{12}$ Kg)	Rainwater evaporation ($\times 10^{12}$ kg)	Total rainfall ($\times 10^{12}$ kg)	Precip. efficiency (%)
($U_s = 10$ m s^{-1} over 2.5 km)					
1	0.71	0.15	0.17	0.32	0.46
2	0.69	0.13	0.15	0.34	0.49
4	0.64	0.12	0.13	0.34	0.52
8	0.64	0.13	0.06	0.34	0.57
12	0.42	0.16	0.03	0.16	0.37
($U_s = 17.5$ m s^{-1} over 2.5 km)					
1	0.77	0.08	0.19	0.42	0.55
2	0.77	0.08	0.18	0.45	0.58
4	0.73	0.09	0.12	0.47	0.64
8	0.63	0.12	0.06	0.37	0.59
12	0.42	0.15	0.04	0.15	0.35
($U_s = 25$ m s^{-1} over 5.0 km)					
1	0.85	0.10	0.17	0.49	0.58
2	0.86	0.10	0.18	0.48	0.56
4	0.66	0.12	0.08	0.39	0.59
8	0.53	0.13	0.04	0.27	0.50
12	0.36	0.15	0.03	0.09	0.25

TABLE 1b. Moisture statistics: $T = 6$ h.

Resolution (km)	Total condensation ($\times 10^{12}$ kg)	Cloud water evaporation ($\times 10^{12}$ Kg)	Rainwater evaporation ($\times 10^{12}$ kg)	Total rainfall ($\times 10^{12}$ kg)	Precip. efficiency (%)
($U_s = 10$ m s^{-1} over 2.5 km)					
1	1.54	0.40	0.33	0.78	0.52
2	1.44	0.36	0.29	0.78	0.54
4	1.36	0.32	0.25	0.79	0.58
8	1.44	0.27	0.24	0.94	0.66
12	1.51	0.29	0.19	1.03	0.68
($U_s = 17.5$ m s^{-1} over 2.5 km)					
1	1.65	0.16	0.41	0.98	0.59
2	1.62	0.20	0.39	1.03	0.64
4	1.60	0.18	0.32	1.12	0.70
8	1.74	0.20	0.26	1.34	0.77
12	1.69	0.25	0.17	1.29	0.77
($U_s = 25$ m s^{-1} over 5.0 km)					
1	1.91	0.21	0.46	1.23	0.64
2	1.97	0.19	0.47	1.27	0.65
4	1.85	0.22	0.31	1.33	0.72
8	1.81	0.22	0.18	1.43	0.79
12	1.72	0.27	0.16	1.29	0.75

heat fluxes observed at this time for these cases (Fig. 11). For the deeper shear, $U_s = 25$ m s^{-1} case, $\overline{q_r}$ near the surface for the coarser resolutions are comparable to the 1-km simulation, but $\overline{q_r}$ aloft at 3 h is as yet much weaker, suggesting again that the coarse-resolution convective systems are much slower to evolve for stronger, deeper vertical wind shears.

By 6 h, the rainwater mixing ratios in the 1-km resolution simulations have all decreased in magnitude, consistent with the general weakening of the convective systems over time. The 2- and 4-km resolution results again compare reasonably well for all three shear cases, while the coarser-resolution simulations are producing substantially more rain. This result parallels the results for the vertical heat fluxes, which were also substantially overpredicted for the coarser resolutions at 6 h (Fig. 11).

The statistics for the moisture processes are summarized in Table 1, which presents the total condensation (integrated over the entire domain and over time), the total evaporation of cloudwater and rainwater, the total rainfall reaching the ground, and the precipitation efficiencies at 3 and 6 h for all of the simulations. Precipitation efficiency is defined to be the total amount of rainfall reaching the ground divided by the total amount of condensation within the full domain. At 3 h (Table 1a), the total precipitation for the $U_s = 10$ m s^{-1} simulations are all comparable, except for the 12-km resolution case, which is much less. As noted previously, the 12-km resolution simulation has yet to develop the mature upshear-tilted structure that is characteristic of the finer-resolution cases by 3 h. The precipitation efficiencies actually increase with decreasing resolution through 8 km, with the 12-km case again showing a significant decrease. The general increase in precipitation efficiency with finer resolution seems most related to a significant decrease in the total evaporation of rainwater for these cases. For the stronger shear simulations at 3 h, there is a systematic decrease in total precipitation along with a similar decrease in rainwater evaporation with decreasing resolution. By 6 h (Table 1b), there is a general increase in total precipitation and precipitation efficiency along with a continuing decrease in rainwater evaporation for decreasing resolution for all three shear experiments.

c. System asymmetries

As discussed previously, it may not be appropriate to apply the above system-averaged profiles to help specify flux magnitudes for a parameterization scheme for use in models with resolutions of the same order or greater than the scale of the convective system. As can be seen from the system-averaged vertical cross sections (e.g., Figs. 5–10), the scale of the present squall lines is such that even a 50-km grid interval would be sufficient to resolve a portion of the mature system-scale structure. Since the convective circulation varies significantly from one side of the system to the other, single flux profiles defined for 50-km grid intervals or less cannot uniquely represent the impact of the convective system on the larger scales of motion.

The basic characteristics of this system asymmetry are depicted in Fig. 15, which presents vertical profiles of u, θ, and q_v averaged over 100-km intervals extending to both the east and west of the leading edge of the

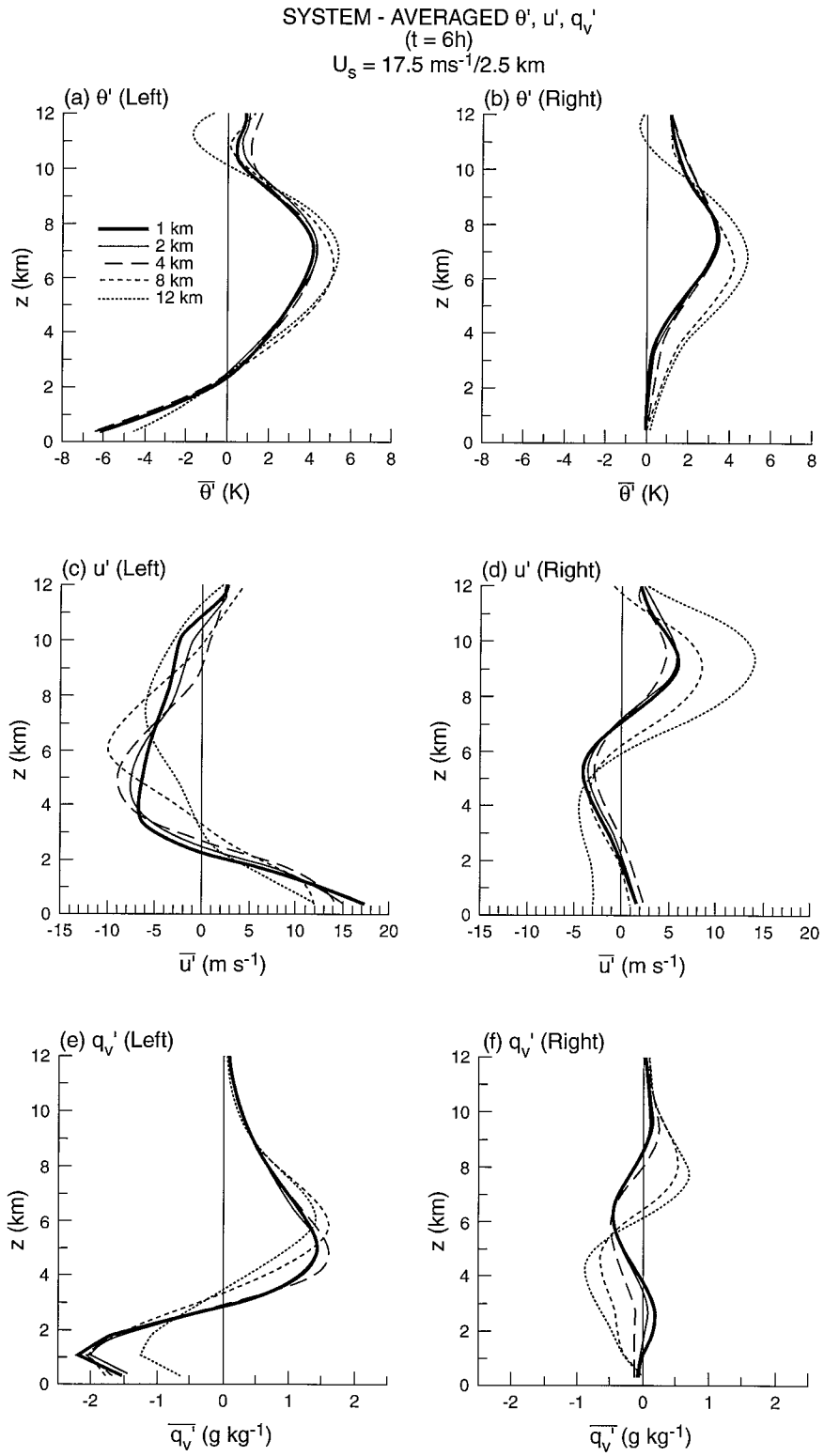

FIG. 15. Line-averaged vertical profiles of (a, b) θ', (c, d) u', and (e, f) q_v' extending 100 km to the left and right of the surface cold-pool boundary, respectively, for the $U_s = 17.5$ m s^{-1} (2.5 km)$^{-1}$ simulation at 6 h. The 1-km resolution simulation is depicted by a thick solid line, 2 km by a thin solid line, 4 km by a large-dashed line, 8 km by a small-dashed line, and 12 km by a dotted line.

surface gust front for the $U_s = 17.5$ m s^{-1} shear case at 6 h. To the west of the surface gust front (Figs. 15a,c,e), the vertical profiles reflect a warm and moist ascending front-to-rear updraft current above a cold and dry descending rear-inflow current, as is characteristic of a mature squall line. To the east of the surface gust front (Figs. 15b,d,f), the profiles are quite different, now reflecting easterly anvil outflow aloft with subsidence warming beneath. Thus, single column profiles of heat, momentum, or moisture do not reflect the system asymmetries that would be important to capture in a convective parameterization scheme.

5. The resolution dependence of the convective processes

The degradation of results evident in the coarser-resolution simulations may be due to a host of different effects, ranging from the inappropriateness of the cloud microphysics and mixing parameterizations applied at the coarser resolutions, to simply the inability of the coarser resolutions to resolve smaller-scale effects that govern the evolution of the convective system. Implicit in this latter effect is the ability of the model equations to properly represent nonhydrostatic motions for a specified resolution. Standard scaling analyses of the equations of motion confirm that nonhydrostatic effects are clearly significant for motion scales of a few kilometers or less, but are generally not significant for motion scales of tens of kilometers or greater. Thus, as the horizontal grid size within a ''nonhydrostatic'' numerical model is varied between 1 and 12 km, the effective model physics range from a fully nonhydrostatic to an effectively hydrostatic characterization of the system evolution. Another concern is the slower evolution of the convective cold pool for coarser resolutions, which further regulates the timing of the evolution of the convective system. In this section, we will address these issues in more detail in an attempt to understand the resolution dependencies that are evident in our set of simulations.

a. Hydrostatic versus nonhydrostatic effects

There are two aspects of the transition between hydrostatic and nonhydrostatic processes that may have particular bearing on the interpretation of the resolution dependencies described above. First, nonhydrostatic processes will tend to limit the magnitude of the vertical mass transports that would be produced in an equivalent, hydrostatic simulation. This helps to explain, for instance, why the coarser-resolution simulations produce overall stronger circulations than the fine-resolution cases. The second aspect is that the timescale for the evolution of hydrostatic disturbances tends to increase with increasing length scale. Thus, as the resolution for a simulation is decreased within the hydrostatic range of motions, the evolution of the simulated system should be characteristically slower.

The basic nature of the transition between the physics of hydrostatic versus nonhydrostatic motions is contained in the linearized, two-dimensional, Boussinesq equations of motion:

$$\frac{\partial}{\partial t}\left(\frac{\partial u}{\partial z} - \frac{\partial w}{\partial x}\right) = \frac{-\partial B}{\partial x} \tag{1}$$

$$\frac{\partial u}{\partial x} + \frac{\partial w}{\partial z} = 0 \tag{2}$$

$$\frac{\partial B}{\partial t} = -N^2 w, \tag{3}$$

where B is the buoyancy, N is the Brunt–Väisälä frequency, and where it has been assumed, for simplicity, that there is no moisture, friction, Coriolis effects, or mean wind. This system of equations is commonly used to characterize the properties of internal gravity waves (e.g., Holton 1992; Lilly 1960). By formulating an equation for w and assuming usual normal mode solutions, one can derive the following relationship between the amplitude of the normal modes, W_0 and B_0:

$$W_0 \approx \frac{k}{(k^2 + l^2)^{1/2} N} B_0, \tag{4}$$

where $k = 2\pi/\lambda_x$ and $l = 2\pi/\lambda_z$ are the horizontal and vertical wavenumbers, respectively. For hydrostatic motions, the horizontal wavelength is assumed to be much larger than the vertical wavelength, leading to

$$W_0 \approx \frac{\lambda_z}{\lambda_x N} B_0 \approx \frac{1}{\lambda_x} \frac{H}{N} B_0, \tag{5}$$

where H represents a standard scale height.

This relationship demonstrates one of the basic characteristics of hydrostatic motions: that the amplitude of the vertical motion scales directly as the inverse of the horizontal wavelength. Thus, as the horizontal scale of motion gets smaller, the amplitude of the vertical motion increases proportionally. Equivalently, as the grid scale is reduced in a hydrostatic model (thus allowing the model to represent smaller scales of motion), the resultant vertical motions for a given disturbance would also be expected to increase proportionally.

The most crucial difference physically between the hydrostatic and nonhydrostatic systems is that for the nonhydrostatic system, the vertical motions are more restricted in their rate of increase for decreasing wavelength, due to the additional term involving the horizontal wavenumber in the denominator of Eq. (4). This relationship can also be expressed in terms of vertical mass flux, m, which is proportional to W_0/k. For hydrostatic motions, $m_h \approx B_0/lN$, while for nonhydrostatic motions, $m_{nh} \approx B_0/(k^2 + l^2)^{1/2}N$. Thus, for a given vertical scale, the vertical mass flux is independent of horizontal wavenumbers for hydrostatic motions, but de-

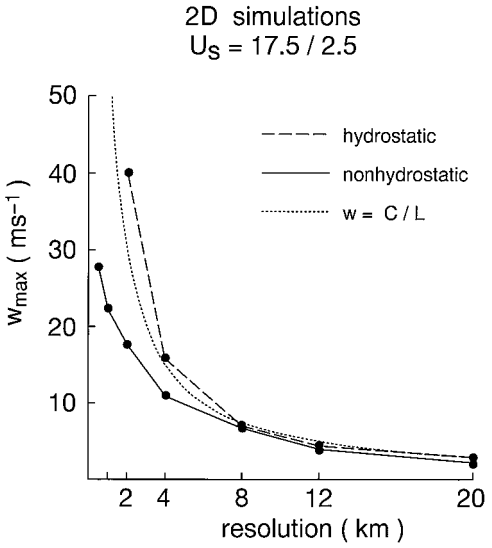

FIG. 16. Maximum vertical velocities obtained for the various-resolution two-dimensional simulations for the full nonhydrostatic (solid) and an equivalent hydrostatic (dashed) model. The dotted line represents the estimated vertical velocity for a purely hydrostatic model, assuming a $1/\Delta x$ scaling and a vertical velocity of 3 m s^{-1} at 20-km resolution.

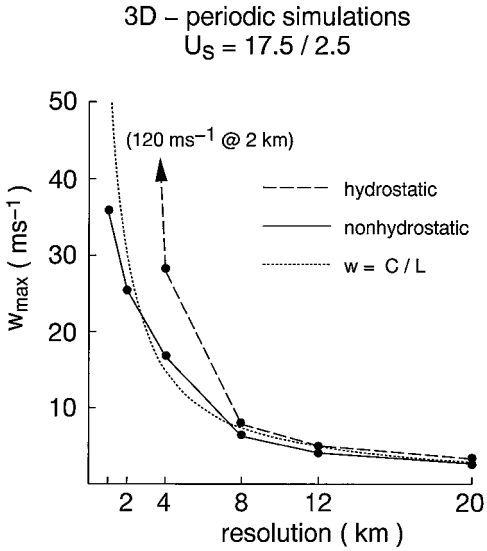

FIG. 17. Maximum vertical velocities obtained for the various-resolution three-dimensional simulations for the full nonhydrostatic (solid) and an equivalent hydrostatic (dashed) model. The dotted line represents the estimated vertical velocity for a purely hydrostatic model, assuming a $1/\Delta x$ scaling and a vertical velocity of 3 m s^{-1} at 20-km resolution.

creases with increasing wavenumber for nonhydrostatic motions. This result is consistent with the overprediction of the vertical mass flux in the coarser-resolution simulations discussed in the previous section. In the simulations with coarse resolution, the horizontal wavenumbers are artificially small. Thus, the vertical velocity magnitudes as described by Eq. (4) will be artificially large, behaving more like the hydrostatic system described by Eq. (5). These relationships between hydrostatic versus nonhydrostatic vertical momentum or vertical mass flux have also been discussed recently by Orlanski (1981) and Kato and Saito (1995).

Although this analysis has been derived for a system of equations much simpler than the full moist, nonlinear equations used in the simulations, we can show that these relationships are still relevant to the more complicated system. For this purpose, we have plotted maximum vertical velocity versus resolution for two sets of simulations: the set of three-dimensional nonhydrostatic simulations described previously (Fig. 17) as well as an equivalent set of two-dimensional nonhydrostatic simulations (Fig. 16), both for the $U_s = 17.5$ m s^{-1} shear case. The two-dimensional simulations have been included to compare more directly to the two-dimensional analysis described above. Equivalent hydrostatic simulations have also been run for each set to more clearly delineate the transition from hydrostatic to nonhydrostatic regimes. For this purpose, 20-km resolution simulations have also been included to expand the results further into the hydrostatic regime, but the timescale for these runs was prohibitively long to warrant other comparisons with the finer-resolution simulations. A projected maximum vertical velocity assuming hydrostatic scaling of $1/\Delta x$ for a baseline vertical velocity of 3 m s^{-1} at 20-km resolution has been added to both figures for comparison.

For the two-dimensional cases (Fig. 16), the maximum vertical velocities for the hydrostatic simulations increase in magnitude for decreasing grid size at a rate that is quite comparable to the rate based on pure hydrostatic scaling of the simplified equations. Results for the three-dimensional hydrostatic simulations are also comparable (Fig. 17), except that the rate of increase of the maximum vertical velocities for decreasing grid size is even larger, most likely due to three-dimensional influences not included in the two-dimensional scaling arguments. The maximum vertical velocities for both the two-dimensional and three-dimensional nonhydrostatic simulations are comparable to those for the hydrostatic simulations for grid resolutions of 8 km or larger, but are significantly weaker than the hydrostatic simulations for grid resolutions less than 8 km. Thus, 8 km represents the grid spacing for these cases beyond which nonhydrostatic simulations become effectively hydrostatic.

In addition to the influence on vertical mass transports, the transition from fine to coarse resolutions should naturally result in a slower evolution to the convective system. This relationship can easily be deduced from the dispersion relation for the set of equations described above: that is,

$$\omega = \frac{kN}{(k^2 + l^2)^{1/2}}, \tag{6}$$

which, for hydrostatic motions, reduces to

$$\omega = \frac{kN}{l}. \tag{7}$$

Thus, $\omega \approx k$, which shows that the timescale (frequency) of a disturbance will increase (decrease) as the wavelength (wavenumber) increases (decreases). If k is artificially too small, as occurs for the coarse-resolution simulations, then the frequency will be artificially decreased and the timescale will be artificially increased.

b. *The resolution dependency of the evolving cold pool*

For a given resolution, the timing of the evolution of a convective system also depends strongly on the strength of the convectively produced cold pool. In particular, the transition from the downshear to an upshear-tilted structure does not commence until the cold-pool-generated circulation is strong enough to overcome the opposing circulation in the ambient shear (e.g., RKW, WKR). As described in RKW, the strength of the cold pool circulation can be represented by calculating the integrated buoyancy deficit, which also reflects the theoretical speed of propagation of a cold pool in an initially calm environment:

$$C^2 = 2\int_0^H (-B)\, dz, \tag{8}$$

where B represents the full buoyancy, given by

$$B \equiv g\left[\frac{\theta'}{\bar{\theta}} + 0.61(q_v - \bar{q}_v) - q_c - q_r\right], \tag{9}$$

where θ is the potential temperature, and q_v, q_c, and q_r are the mixing ratios of water vapor, cloud water, and rainwater, respectively. A time history of the derived theoretical cold-pool propagation speed (strength) C for all shear and resolution experiments is presented in Fig. 18. Since the cold-pool characteristics vary significantly along the squall line, we choose to estimate C by using the along-line averaged minimum buoyancy and average cold-pool depth as found within the closest 50 km of the leading edge of the system. These estimates vary by as much as 2 m s^{-1} at particular points along the line, but the differences in magnitudes among the various simulations are still large enough to highlight systematic differences among the cases.

For all three shear cases, the 1-km resolution simulations depict a decline in cold-pool strength during the initial hour, followed by a significant increase in C from 1 to 3 h. The initial decrease is due to the weakening of the initial pool of cold air as it subsides and mixes with the ambient air. The subsequent strengthening then occurs as the triggered convective cells produce cold outflows that enhance the cold pool. In all three cases, the mature, steady-state cold pool becomes stronger than the cold pool specified in the initial state.

In the 4-km simulations, the strengthening of the cold pool after the initial hour is delayed, but eventually reaches strengths comparable to those produced in the 1-km simulations. The 8-km simulations are further delayed and eventually recover to the 1-km result only for the weak and moderate shallow-shear simulations. Finally, the 12-km cold pools remain significantly weaker than the 1-km cold pools for all three shear cases throughout the 6-h simulations. All in all, the best comparison in cold-pool strength at 6 h for the differing resolutions occurs with the weakest shear case, and becomes progressively worse for stronger and deeper shears.

There are several factors that may contribute to the

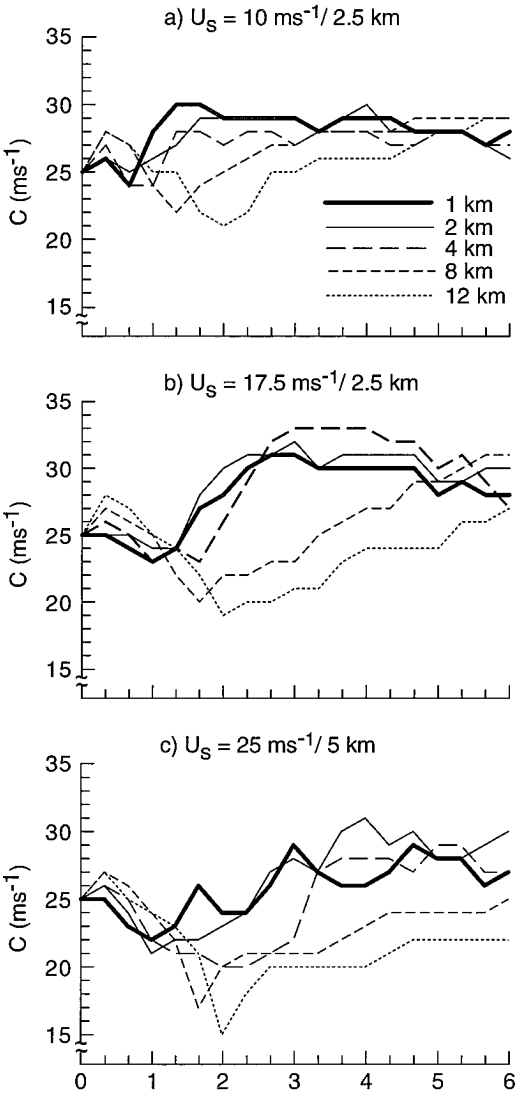

FIG. 18. Average derived theoretical cold-pool propagation speed C for the various resolution simulations for (a) U_s = 10 m s^{-1} (2.5 km)$^{-1}$, (b) U_s = 17.5 m s^{-1} (2.5 km)$^{-1}$, and (c) U_s = 25 m s^{-1} (5 km)$^{-1}$ simulations, respectively. The 1-km resolution simulation is depicted by a thick solid line, 2 km by a thin solid line, 4 km by a large-dashed line, 8 km by a small-dashed line, and 12 km by a dotted line.

delayed or weakened cold pools in the coarse-resolution simulations. The delayed strengthening may simply be due in part to the inherently longer timescale for evolution that would be expected for the coarser resolutions, as described above. However, since the coarse-resolution simulations eventually produce rainfall rates much larger than the fine-resolution simulations, one might expect even more evaporation and a stronger cold pool in the coarse-resolution simulations. As shown in Table 1b, though, the coarse-resolution simulations are also characterized by much less rainfall evaporation over the 6-h period, which results in larger precipitation efficiencies as well. The reduction in evaporation may also be responsible somewhat for the reduced net drying at low levels for the coarse-resolution simulations (Fig. 13), due to the reduction in strength of the descending rear-inflow current.

The descending rear-inflow current is important in this regard in that it transports low θ_e from midlevels into the surface cold pool, which directly controls the amount of evaporation and net cooling experienced by descending air parcels. For the present sounding (Fig. 1), air parcels that experience saturated descent from 750 mb to the surface would evaporate 4.5 g kg^{-1} of rainwater, leading to a surface temperature deficit of 7 K. An ambient surface air parcel, however, could potentially evaporate less than 2 g kg^{-1} of rainwater, leading to a surface temperature deficit of only 4 K. Thus, the ability of the coarse-resolution simulations to generate sufficiently deep downdrafts is critical to reproducing the finer-resolution results.

To better document this process for the various shear and resolution simulations, line-averaged vertical profiles of θ_e at 3 and 6 h are presented in Fig. 19. For this purpose, the averaging has been taken over a 100-km area extending rearward from the leading edge of the surface gust front to emphasize the cold-pool characteristics. At 3 h, there is good correspondence among the θ_e profiles for the 1-, 2-, and 4-km simulations for both of the shallow-shear cases, and good correspondence between the 1- and 2-km results for the deeper shear case. The θ_e's over the lowest several kilometers in the coarser-resolution simulations, however, are significantly warmer, confirming the lack of a sufficiently strong or deep downdraft current at this time. Consistent with the previous analysis of cold-pool strength (e.g., Fig. 17), the low-level θ_e comparisons improve considerably by 6 h, with the exception of the stronger and deeper-shear 12-km resolution simulations, which still show near-surface θ_e's as much as 5 K too warm.

One possible reason for the lack of a sufficiently deep and strong cold pool in the coarser-resolution simulations may be related directly to the microphysical parameterization itself. Specifically, the terminal fall velocity of rainwater in the Kessler scheme being employed is merely a function of the rainwater mixing ratio, which does not scale with the horizontal resolution. In fact, despite weaker vertical velocities, the average rainwater mixing ratios for the coarse-resolution simulations are actually larger than for the fine-resolution cases (Fig. 14). This leads to a more rapid fallout of the rain in the coarser-resolution cases, which could contribute to a reduction in net evaporation of rain as well (Table 1). Similar concerns were also raised by Zhang et al. (1989), who found it necessary to reduce the terminal fall velocities by 70% to produce realistic results in a 25-km horizontal grid resolution simulation of the 10–11 June 1985 squall line.

To test this hypothesis, a series of simulations were run for the 12-km resolution $U_s = 17.5$ m s^{-1} shallow-shear case with the terminal fallspeed of the rain reduced by factors of 0.75, 0.5, and 0.25. The impact of these modifications to the moisture statistics and resultant cold-pool strengths are presented in Table 2. The original 1-km resolution statistics are also included for comparison. These results suggest that a reduction in the rainwater fallspeed does significantly increase the amount of rainwater evaporation in the 12-km resolution simulations over the second 3 h of the simulations, leading to stronger cold pools over this period as well. It also results in a reduction of net rainfall and precipitation efficiency over 6 h for fallspeed reductions of 50% or greater, leading to a better comparison with the 1-km results. This apparent improvement in the 12-km resolution simulations by 6 h, however, is at the expense of even worse comparisons with the 1-km results during the first 3 h of the simulations. This suggests that modifications to the rainwater fallspeed alone are not sufficient to speed up the evolution of the coarser-resolution simulations.

6. Summary and discussion

The present results suggest that resolutions within nonhydrostatic models as coarse as 4 km may be sufficient to reproduce the mesoconvective circulations and net momentum and heat transports of midlatitude type convective systems. For 8- and 12-km resolutions, certain overall aspects of the circulation and transports are still reasonably represented, but the timescale of the convective evolution is much slower, with the net heat transports, rainfall rates, and net strength of the system-scale circulation significantly larger than in the finer-scale simulations. The ability of the coarse-resolution simulations to generate at least qualitatively similar circulations seems to stem from the fact that even within the fine-resolution simulations, the circulation produced during the mature phase of the convective system is largely hydrostatic, as the cold pool at the surface and warm perturbations aloft expand in size and produce mesoscale pressure fields that sustain the flow. The relative slowness of the evolution in the coarse resolution cases seems most related to the slower strengthening of the cold pool, due to a weaker descending rear-inflow current.

The overprediction of the heat transports, rainfall

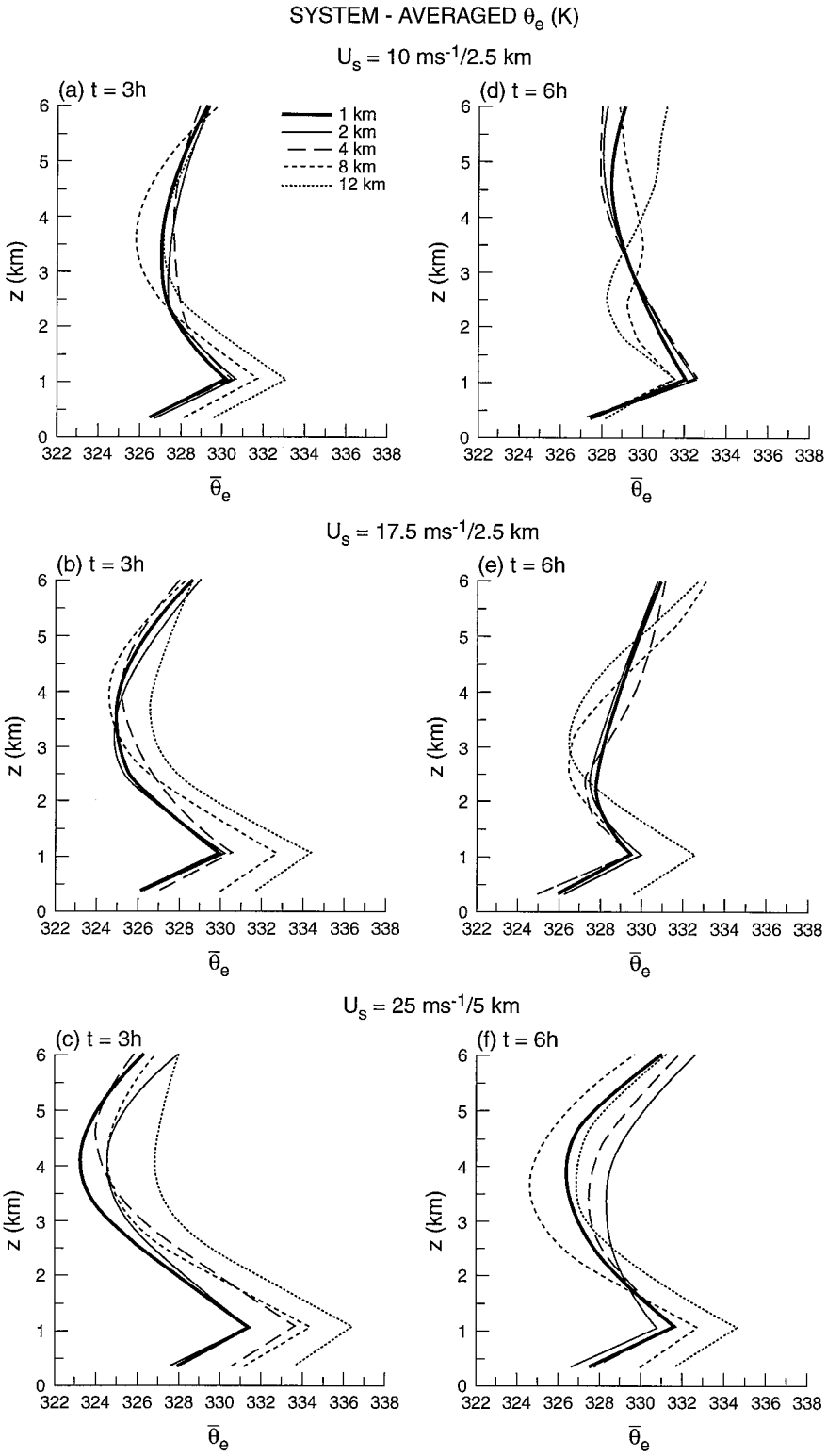

FIG. 19. Line-averaged vertical profiles of θ_e for resolutions of 1, 2, 4, 8, and 12 km for the (a, d) U_s = 10 m s^{-1} (2.5 km)$^{-1}$, (b, e) U_s = 17.5 m s^{-1} (2.5 km)$^{-1}$, and (c, f) U_s = 25 m s^{-1} (5 km)$^{-1}$ simulations at 3 and 6 h, respectively. The 1-km resolution simulation is depicted by a thick solid line, 2 km by a thin solid line, 4 km by a large-dashed line, 8 km by a small-dashed line, and 12 km by a dotted line. All averages are calculated over a 100-km area extending rearward from the surface cold-pool boundary.

TABLE 2. Fall velocity sensitivities (U_s = 17.5 m s^{-1} over 2.5 km).

Fall velocity (V_R)	Total condensation ($\times 10^{12}$ kg)	Rainwater evaporation ($\times 10^{12}$ kg)	Total rainfall ($\times 10^{12}$ kg)	Precip. efficiency (%)	C (m s^{-1})
(T = 3 h)					
1 km	0.77	0.19	0.42	0.55	31
12 km					
V_R	0.42	0.04	0.15	0.35	21
$0.75V_R$	0.41	0.04	0.13	0.31	22
$0.50V_R$	0.40	0.05	0.08	0.21	22
$0.25V_R$	0.38	0.06	0.00	0.00	23
(T = 6 h)					
1 km	1.65	0.41	0.98	0.59	28
12 km					
V_R	1.69	0.17	1.29	0.77	27
$0.75V_R$	1.64	0.19	1.23	0.75	28
$0.50V_R$	1.60	0.24	1.10	0.69	28
$0.25V_R$	1.49	0.32	0.75	0.51	32

rates, and system-scale circulation within the coarse-resolution simulations seem consistent with results reported for other recent explicit mesoscale simulations of convective systems reported in the literature. For instance, for an MCC case, Zhang et al. (1988) found that a purely explicit simulation resulted in the production of too much rain as well as too intense a surface mesolow for both 12.5- and 25-km resolutions. Using 14-km resolution, Tripoli (1986) and Tripoli et al. (1986) similarly found an excessive production of rain and a spuriously intense mesoscale convective system for a convective event. Kato and Saito (1995) varied the resolution between 5, 10, and 20 km for explicit simulations of a convective cell, and also found that hydrostatic simulations overdeveloped the moist convection, overestimated the total amount of precipitation, and overexpanded the area of precipitation as the grid size increased. As noted herein and also by Kato and Saito (1995), this overprediction seems most related to the inability of the coarse-resolution simulations to properly represent nonhydrostatic effects, which would limit the growth of the convective updrafts.

The present results suggest that convective parameterization schemes designed for mesoscale models with horizontal grid intervals less than 20 km must somehow account for both the overprediction of the vertical mass transport, which results from insufficient representation of the nonhydrostatic effects, and the underprediction of the convectively generated cold pool, which results from the apparent inability of the downdrafts within the coarser-resolution simulations to transport low-θ_e air to the surface in a timely manner. The proper representation of the cold pool is especially important in this regard to properly reproduce the overall character of the mesoconvective system, including the upscale growth and the associated vertical momentum and heat flux profiles. The present results emphasize that the strength of the ambient vertical wind shear provides an additional control on the timing of system evolution as well as the resultant shape and magnitudes of the various flux profiles. In general, the accuracy of explicitly simulated convective systems with coarse resolution decreases with increasing magnitudes of vertical wind shear. To the authors' knowledge, no current convective parameterization scheme accounts for the impacts of vertical wind shear on convective system evolution, except for the determination of precipitation efficiency (e.g., Fritsch and Chappell 1980).

A concern that arises in trying to formulate convective parameterization schemes is whether momentum fluxes characteristic of the mature phase of a convective system need to be included in addition to the usual heat and moisture fluxes (e.g., Moncrieff 1992). While this may indeed be necessary for parameterization schemes designed for very coarse-resolution models, the present results emphasize that the mature circulation that is used to characterize such momentum flux profiles will indeed be generated (albeit slowly) by the resolved sources and sinks of buoyancy (i.e., potential temperature perturbations) within the system with resolutions as coarse as 12 km. In fact, the mature circulations produced in these coarse-resolution simulations are actually overpredicted, despite the initial underprediction of the momentum fluxes.

The results reported herein are derived for thermodynamic and vertical wind shear environments most often associated with strong, midlatitude squall-line-type systems. Thus, the conclusions may not be applicable to convective systems evolving in different environments or that exhibit a different type of organization. For instance, numerical studies of tropical convection, for which the CAPE is often much less than that associated with the midlatitude cases, have generally had to use smaller horizontal grid resolutions to properly resolve the weaker convective updrafts and downdrafts. Thus, the 4-km minimal resolution necessary to resolve the system-scale properties for the midlatitude environments may have to be reduced for tropical environments. The present results may similarly need to be adjusted for more disorganized convective systems, for which there is no clear internal mechanism for upscale growth as is evident in the present shear-perpendicular squall lines.

Recent observational and numerical studies also reveal the importance of three-dimensional structures, such as mesoscale convective vortices, in the evolution of some longer-lived convective systems (e.g., Houze et al. 1990; Skamarock et al. 1994). The long-term evolution of such systems may actually be easier to resolve in mesoscale models due to their more balanced dynamical nature (e.g., Davis and Weisman 1994). However, preliminary simulations for both fine and coarse resolutions with the Coriolis forcing included suggest that the enhanced circulation noted for the coarse-resolution quasi-two-dimensional squall lines may result likewise in the overdevelopment of mesoscale convec-

tive vortices in fully three-dimensional convective systems.

Another valid concern is whether the use of a 1-km grid is sufficient to truly represent the ''ground truth'' solution by which the coarser-resolution simulations can be judged. Clearly, the 1-km solution has not converged in the sense that details of the solution will not change significantly as the grid interval is decreased further. For instance, the maximum vertical velocities for the nonhydrostatic simulations depicted in Fig. 17 are still increasing steadily as the grid interval decreases from 2 to 1 km. Indeed, recent studies suggest that grid resolutions of 500 m or less may be needed to properly resolve the detailed cellular-scale features within a convective system (e.g., Droegemeier et al. 1994). However, the system-scale features do seem to be reasonably converged, as revealed by the comparison of the system averaged flux profiles of heat, momentum, etc. (e.g., Figs. 11–14). Given the nature of these models with parameterized turbulence and microphysics, it is in this system-averaged sense that we have the most confidence in our conclusions.

Several important issues related to convective parameterizations are not addressed by this study. Perhaps foremost is the issue of convective triggering, which we have intentionally avoided through the use of an initial cold pool strong enough to trigger convection for all of the resolution and vertical wind shear cases we have considered. In reality, a successful forecast of convection relies ultimately on the ability of a mesoscale model to accurately forecast the onset of convective activity, whether the simulation is fully explicit or parameterized. Second, the lack of ice microphysics in the present simulations may also affect the accuracy of our findings. However, while many studies point to the importance of ice microphysics in the longer-term evolution of convective systems and their impact on the larger-scale environment, these effects are much less over the 6-h timescales used in the present study.

In their review of convective precipitation within mesoscale models, Molinari and Dudek (1992) note that before cumulus parameterizations can be widely used in high-resolution mesoscale models, more detailed analysis of why convective parameterizations succeed and fail is needed. We hope that we have presented a useful step in this process by more clearly identifying what goes wrong in explicit simulations of convective systems with coarse resolutions and by identifying those physical processes most responsible for the deteriorating results.

Acknowledgments. We would like to gratefully acknowledge valuable discussions and reviews of this manuscript by Richard Rotunno, Ying-Hwa Kuo, Jimy Dudhia, Scott Braun, Mitchell W. Moncrieff, and two anonymous reviewers.

APPENDIX

Sensitivities to Physical and Numerical Mixing

As discussed in section 2, it is difficult to formulate the numerical and physical mixing for these resolution experiments so that the choice of mixing parameters will not significantly impact the resolution dependencies. To test the sensitivity of the results to the various mixing formulations that could be applied, we have run additional simulations for the $U_s = 17.5$ m s^{-1}, 4-, 8-, and 12-km resolution cases, using reduced magnitudes of physical and numerical smoothing. Simulations were run with the fourth-order smoothing coefficient F4DMP reduced by a factor of 2 and 10, as well as with the physical mixing coefficient K_m scaled to a 1-km horizontal resolution and also set completely to zero. The results of the 12-km resolution tests, which were also representative of the 4- and 8-km resolution sensitivity tests, are summarized in Table A1, which includes key moisture statistics and the derived theoretical speed of propagation of the system generated cold pool, C, as defined in sections 4b and 5b, respectively. The statistics for the ''ground truth'' 1-km resolution simulations are also included for comparison.

In general, the computational mixing contributes much more to the net smoothing than the physical mixing in these simulations, which is consistent with our past studies as well. For instance, setting K_m to zero had much less effect on the simulations than reducing F4DMP by a factor of 10. However, the cases with F4DMP reduced by a factor of 10 produced gridpoint-type storms, which do not represent a desired, well-resolved solution. All in all, the comparisons between the less-damped coarse-resolution solutions and the fine-resolution statistics were generally worse, with the reduced mixing cases producing much more conden-

TABLE A1. Mixing sensitivities: ($U_s = 17.5$ m s^{-1} over 2.5 km).

Mixing	Total condensation ($\times 10^{12}$ kg)	Rainwater evaporation ($\times 10^{12}$ kg)	Total rainfall ($\times 10^{12}$ kg)	Precip. efficiency (%)	C (m s^{-1})
($T = 3$ h)					
1 km	0.77	0.19	0.42	0.55	31
12 km	0.42	0.04	0.15	0.35	21
0.5(F4DMP)	0.55	0.05	0.27	0.48	22
0.1(F4DMP)	0.83	0.10	0.56	0.67	24
K_m (1 km)	0.51	0.05	0.18	0.35	21
$K_m = 0$	0.34	0.02	0.12	0.36	21
($T = 6$ h)					
1 km	1.65	0.41	0.98	0.59	28
12 km	1.69	0.17	1.29	0.77	27
0.5(F4DMP)	1.72	0.22	1.34	0.78	28
0.1(F4DMP)	1.89	0.33	1.44	0.77	32
K_m (1 km)	2.02	0.21	1.55	0.77	26
$K_m = 0$	1.88	0.21	1.51	0.81	25

sation and rainfall by 6 h than the nominal 12-km case. Thus, the statistical differences between the 1-km and 12-km resolution simulations do not seem to be a function of our choice of mixing formulation.

REFERENCES

Anthes, R. A., 1977: A cumulus parameterization scheme utilizing a one-dimensional cloud model. *Mon. Wea. Rev.*, **105,** 270–286.

Bluestein, H. B., and M. H. Jain, 1985: Formation of mesoscale lines of precipitation: Severe squall lines in Oklahoma during the spring. *J. Atmos. Sci.*, **42,** 1711–1732.

Davis, C. A., and M. L. Weisman, 1994: Balanced dynamics of mesoscale vortices produced in simulated convective systems. *J. Atmos. Sci.*, **51,** 2005–2030.

Droegemeier, K. K., G. Bassett, and M. Xue, 1994: Very high-resolution, uniform-grid simulations of deep convection on a massively parallel computer: Implications for small-scale predictability. Preprints, *10th Conf. on Numerical Weather Prediction*, Portland, OR, Amer. Meteor. Soc., 376–379.

Fovell, R. G., 1991: Influence of the Coriolis force on two-dimensional model storms. *Mon. Wea. Rev.*, **119,** 606–630.

Frank, W. M., 1983: The cumulus parameterization problem. *Mon. Wea. Rev.*, **111,** 1859–1871.

Fritsch, J. M., and C. F. Chappell, 1980: Numerical prediction of convectively driven mesoscale pressure systems. Part 1: Convective parameterization. *J. Atmos. Sci.*, **37,** 1722–1733.

Holton, J. R., 1992: *An Introduction to Dynamic Meteorology*. Academic Press, 511 pp.

Houze, R. A., S. A. Rutledge, M. I. Biggerstaff, and B. F. Smull, 1989: Interpretation of Doppler weather radar displays of midlatitude mesoscale convective systems. *Bull. Amer. Meteor. Soc.*, **70,** 608–619.

——, B. F. Smull, and P. Dodge, 1990: Mesoscale organization of springtime rainstorms in Oklahoma. *Mon. Wea. Rev.*, **118,** 613–654.

Kato, T., and K. Saito, 1995: Hydrostatic and non-hydrostatic simulations of moist convection: Applicability of the hydrostatic approximation to a high-resolution model. *J. Meteor. Soc. Japan*, **73,** 59–77.

Klemp, J. B., and R. B. Wilhelmson, 1978: The simulation of three-dimensional convective storm dynamics. *J. Atmos. Sci.*, **35,** 1070–1096.

——, and D. R. Durran, 1983: An upper boundary condition permitting internal gravity wave radiation in numerical mesoscale models. *Mon. Wea. Rev.*, **111,** 430–444.

——, R. Rotunno, and W. C. Skamarock, 1994: On the dynamics of gravity currents in a channel. *J. Fluid Mech.*, **269,** 169–198.

Lafore, J., and M. W. Moncrieff, 1989: A numerical investigation of the organization and interaction of the convective and stratiform regions of tropical squall lines. *J. Atmos. Sci.*, **46,** 521–544.

Lilly, D. K., 1960: On the theory of disturbances in a conditionally unstable atmosphere. *Mon. Wea. Rev.*, **88,** 1–17.

Molinari, J., and M. Dudek, 1992: Parameterization of convective precipitation in mesoscale numerical models: A critical review. *Mon. Wea. Rev.*, **120,** 326–344.

Moncrieff, M. W., 1992: Organised mesoscale convective systems: Archetypical dynamical models, mass and momentum flux theory, and parameterization. *Quart. J. Roy. Meteor. Soc.*, **118,** 819–850.

Ooyama, K. V., 1971: A theory on parameterization of cumulus convection. *J. Meteor. Soc. Japan*, **49,** 744–756.

Orlanski, I., 1981: The quasi-hydrostatic approximation. *J. Atmos. Sci.*, **38,** 572–582.

Rotunno, R., J. B. Klemp, and M. L. Weisman, 1988: A theory for strong, long-lived squall lines. *J. Atmos. Sci.*, **45,** 463–485.

Schlesinger, R. E., 1990: Feedback of deep moist convection to its near environment as diagnosed from three-dimensional numerical output: Results from an early experiment. *J. Atmos. Sci.*, **47,** 1390–1412.

——, 1994: Heat, moisture, and momentum budgets of isolated deep midlatitude and tropical convective clouds as diagnosed from three-dimensional model output. Part I: Control experiments. *J. Atmos. Sci.*, **51,** 3649–3673.

Skamarock, W. C., M. L. Weisman, and J. B. Klemp, 1994: Three-dimensional evolution of simulated long-lived squall lines. *J. Atmos. Sci.*, **51,** 2563–2584.

Tripoli, G. J., 1986: A numerical investigation of an orogenic mesoscale convective system. Atmos. Pap. 401, 209 pp. [Available from Department of Atmospheric Sciences, Atmospheric Sciences Building, Colorado State University, Fort Collins, CO 80523.]

——, C. Tremback, and W. R. Cotton, 1986: A comparison of a numerically simulated mesoscale system with explicit and parameterized convection. Preprints, *23d Conf. on Cloud Physics and Radar Meteorology*, Snowmass, CO, Amer. Meteor. Soc., j131–j134.

Weisman, M. L., 1992: The role of convectively generated rear-inflow jets in the evolution of long-lived mesoconvective systems. *J. Atmos. Sci.*, **49,** 1826–1847.

——, 1993: The genesis of severe, long-lived bow-echoes. *J. Atmos. Sci.*, **50,** 645–670.

——, J. B. Klemp, and R. Rotunno, 1988: Structure and evolution of numerically simulated squall lines. *J. Atmos. Sci.*, **45,** 1990–2013.

Zhang, D. L., and J. M. Fritsch, 1988: Numerical sensitivity experiments of varying model physics on the structure, evolution, and dynamics of two mesoscale systems. *J. Atmos. Sci.*, **45,** 261–293.

——, E.-Y. Hsie, and M. W. Moncrieff, 1988: A comparison of explicit and implicit predictions of convective and stratiform precipitating weather systems with a meso-beta-scale numerical model. *Quart. J. Roy. Meteor. Soc.*, **114,** 31–60.

——, K. Gao, and D. B. Parsons, 1989: Numerical simulations of an intense squall line during 10–11 June 1985 PRE-STORM. Part 1: Model verification. *Mon. Wea. Rev.*, **117,** 960–994.